PHYSICAL REVIEW D **79,** 114505 (2009)

Nucleon form factors with 2 + 1 flavor dynamical domain-wall fermions

Takeshi Yamazaki,[1,2,*] Yasumichi Aoki,[3] Tom Blum,[1,3] Huey-Wen Lin,[4] Shigemi Ohta,[5,6,3] Shoichi Sasaki,[7] Robert Tweedie,[8] and James Zanotti[8]

(RBC and UKQCD Collaborations)

[1]*Physics Department, University of Connecticut, Storrs, Connecticut 06269-3046, USA*
[2]*Yukawa Institute for Theoretical Physics, Kyoto University, Kyoto 606-8502, Japan*
[3]*RIKEN-BNL Research Center, Brookhaven National Laboratory, Upton, New York 11973, USA*
[4]*Thomas Jefferson National Accelerator Facility, Newport News, Virginia 23606, USA*
[5]*Institute of Particle and Nuclear Studies, KEK, Tsukuba, 305-0801, Japan*
[6]*Physics Department, Sokendai Graduate University of Advanced Studies, Hayama, Kanagawa 240-0193, Japan*
[7]*Department of Physics, University of Tokyo, Hongo 7-3-1, Tokyo 113-0033, Japan*
[8]*School of Physics & Astronomy, The University of Edinburgh, Edinburgh EH9 3JZ, United Kingdom*
(Received 16 April 2009; published 29 June 2009)

We report our numerical lattice QCD calculations of the isovector nucleon form factors for the vector and axial-vector currents: the vector, induced tensor, axial-vector, and induced pseudoscalar form factors. The calculation is carried out with the gauge configurations generated with $N_f = 2 + 1$ dynamical domain-wall fermions and Iwasaki gauge actions at $\beta = 2.13$, corresponding to a cutoff $a^{-1} = 1.73$ GeV, and a spatial volume of $(2.7\ \mathrm{fm})^3$. The up and down-quark masses are varied so the pion mass lies between 0.33 and 0.67 GeV while the strange quark mass is about 12% heavier than the physical one. We calculate the form factors in the range of momentum transfers, $0.2 < q^2 < 0.75\ \mathrm{GeV}^2$. The vector and induced tensor form factors are well described by the conventional dipole forms and result in significant underestimation of the Dirac and Pauli mean-squared radii and the anomalous magnetic moment compared to the respective experimental values. We show that the axial-vector form factor is significantly affected by the finite spatial volume of the lattice. In particular in the axial charge, g_A/g_V, the finite-volume effect scales with a single dimensionless quantity, $m_\pi L$, the product of the calculated pion mass and the spatial lattice extent. Our results indicate that for this quantity, $m_\pi L > 6$ is required to ensure that finite-volume effects are below 1%.

DOI: 10.1103/PhysRevD.79.114505 PACS numbers: 11.15.Ha, 11.30.Rd, 12.38.Aw, 12.38.Gc

I. INTRODUCTION

The isovector nucleon form factors are probes for nucleon structure associated with the isovector vector and axial-vector currents, $V_\mu^+ = \bar{u}\gamma_\mu d$ and $A_\mu^+ = \bar{u}\gamma_\mu\gamma_5 d$, with up- and down-quark spinors u and d. From these currents, four isovector form factors arise: the Dirac (F_1) and Pauli (F_2) form factors from the vector current,

$$\langle p|V_\mu^+(x)|n\rangle = \bar{u}_p\left[\gamma_\mu F_1(q^2) + \frac{\sigma_{\mu\lambda}q_\lambda}{2M_N}F_2(q^2)\right]u_n e^{iq\cdot x}, \tag{1}$$

where F_1 is equivalent to F_V and $F_2/(2M_N)$ to F_T in the isovector part of the vector and induced tensor form factors in neutron β decay under the isospin symmetry, and they are related to the Sachs electromagnetic form factors

$$G_E(q^2) = F_1(q^2) - \frac{q^2}{4M_N^2}F_2(q^2), \tag{2}$$

$$G_M(q^2) = F_1(q^2) + F_2(q^2), \tag{3}$$

and the axial (F_A) and induced pseudoscalar (F_P) form factors from the axial-vector current,

$$\langle p|A_\mu^+(x)|n\rangle = \bar{u}_p[\gamma_\mu\gamma_5 F_A(q^2) + iq_\mu\gamma_5 F_P(q^2)]u_n e^{iq\cdot x}. \tag{4}$$

We use the Euclidean metric convention as in the recent RBC works [1,2]. Thus q^2 stands for Euclidean four-momentum squared and corresponds to the timelike momentum squared since $q_M^2 = -q^2 < 0$ in Minkowski space. Here $q = p_n - p_p$ is the momentum transfer between the proton (p) and neutron (n).

The vector-current form factors have been studied experimentally with high accuracy at both small ($< 1\ \mathrm{GeV}^2$) and large ($> 1\ \mathrm{GeV}^2$) momentum transfers, through electron elastic scattering off proton and nuclei [3]. Early experiments revealed that the proton is a composite particle [4–7]: i.e. nonzero Pauli and Dirac mean-squared radii and anomalous magnetic moments were measured among other observables. Recent experiments have improved the

*Present address: Center for Computational Sciences, University of Tsukuba, Tsukuba, 305-8577, Japan.

accuracy of these form factors and deviations from earlier perturbative QCD predictions have been observed [8,9].

As is well known, the isovector axial-vector current is strongly affected by the spontaneous chiral symmetry breaking in the strong interaction [10,11]. A consequence for the nucleon is that the isovector axial charge g_A deviates from the corresponding vector charge g_V. These isovector vector and axial-vector charges, respectively, the vector and axial-vector form factors at the zero momentum transfer, are most accurately measured in neutron beta decay experiments: $g_A/g_V = F_A(0)/F_V(0) = 1.2695(29)$ [12]. Whether lattice QCD calculations can accurately reproduce this ratio, g_A/g_V, is an important test of lattice QCD.

The spontaneous breaking of chiral symmetry also means that the corresponding form factors of the axial-vector current are strongly coupled with the Nambu-Goldstone particles, i.e. the pions. Using the axial Ward-Takahashi identity and the pion-pole dominance assumption on the induced pseudoscalar, one can derive the Goldberger-Treiman relation [13], which relates the nucleon mass (M_N), the axial charge (g_A), the pion decay constant (F_π), and the pion-nucleon coupling ($g_{\pi NN}$): $M_N g_A = F_\pi g_{\pi NN}$. It is an interesting challenge for lattice QCD if it can reproduce this relation.

The q^2 dependence of the axial-vector form factor has also been studied in experiments [14]. It again provides a stringent test of QCD through a comparison of lattice QCD calculations with such experiments. While recent experiments report the induced pseudoscalar form factors [15,16], it is less well known than the other form factors. Hence this provides an excellent opportunity for lattice QCD to play a leading role and guide future experiments.

In the past years, many lattice QCD studies have been made for these isovector form factors in the above-mentioned contexts [17,18]. Many earlier works [1,19–22] were performed either in the quenched approximation, neglecting dynamical sea-quark effects or were either limited to two dynamical flavors of Wilson fermion quarks that explicitly violate chiral symmetry [23–25], limited to a nonunitary combination of valence and sea quarks [26–29], or just two dynamical flavors of domain-wall fermions (DWFs) [2]. There has also been an increasing amount of interest in the form factors of other baryons [27,30–33].

In this paper we present our results with more realistic "2 + 1 flavor" dynamical quarks: reasonably light and degenerate up and down quarks and strange quark with a realistic mass are all described by the DWF scheme [34–38] that preserves the flavor and chiral symmetries sufficiently. Earlier studies were often performed on small spatial volumes ($\sim (2\ \mathrm{fm})^3$) which are now widely regarded to be too small to accommodate a nucleon at light quark masses that yield realistic axial charge [24,39]. We use larger spatial lattice volume, as large as 2.7 fm across, to better address the finite-size question.

The rest of the paper is organized as follows: We explain our method of calculation in Sec. II. In Sec. III we first summarize the numerical lattice QCD ensembles used for this work. Then we discuss in detail the known systematic errors in the relevant form factors calculated on these ensembles. The numerical results are presented in Sec. IV. Finally, we give the conclusions in Sec. V.

Since we vary only light quark mass in our simulation while the strange quark mass is fixed, in the following we call the light up and down-quark mass as quark mass, m_f, in the lattice unit, unless explicitly stated otherwise. We note that some preliminary results from this study were presented in Refs. [39–41].

II. METHOD

A. Two- and three-point functions

Following earlier studies with quenched and two dynamical flavors [1,2], we define the two-point function of proton

$$C_S(t - t_{\mathrm{src}}, p) = \frac{1}{4}\sum_{\vec{x}} e^{i\vec{p}\cdot\vec{x}}\,\mathrm{Tr}[\mathcal{P}_4\langle 0|\chi_S(\vec{x}, t)\bar{\chi}_G(\vec{0}, t_{\mathrm{src}})|0\rangle], \tag{5}$$

where S is the index of the smearing of the quark operator and t_{src} is the time location of the source operator. The projection operator $\mathcal{P}_4 = (1 + \gamma_4)/2$ eliminates the contributions from the opposite-parity state for $p^2 = 0$ [42,43]. We use the standard proton operator,

$$\chi_S(x) = \epsilon_{abc}([u_a^S(x)]^T C\gamma_5 d_b^S(x))u_c^S(x), \tag{6}$$

where C is the matrix of the charge conjugation, and a, b, c are color indices, to create and annihilate proton states. In order to improve the overlap with the ground state, we apply Gaussian smearing [44] at the source, while at the sink we employ both local and Gaussian-smeared operators, $S = L$ or G.

In this paper we measure the nucleon isovector matrix elements for the vector and axial-vector currents,

$$\langle p|V_\mu^3(x)|p\rangle = \langle p|\bar{u}(x)\gamma_\mu u(x) - \bar{d}(x)\gamma_\mu d(x)|p\rangle, \tag{7}$$

$$\langle p|A_\mu^3(x)|p\rangle = \langle p|\bar{u}(x)\gamma_5\gamma_\mu u(x) - \bar{d}(x)\gamma_5\gamma_\mu d(x)|p\rangle. \tag{8}$$

While we employ the local currents in most of the calculations, the point-split conserved vector current [38] is used for the vector charge at the lightest quark mass which will be described later.

In order to obtain the matrix elements, we define the three-point function with the current J and the projector $\mathcal{P}_\alpha$

$$C^{\mathcal{P}_\alpha}_{J_\mu}(\vec{q}, t) = \frac{1}{4}\sum_{\vec{x},\vec{z}} e^{i\vec{q}\cdot\vec{z}} \times \mathrm{Tr}[\mathcal{P}_\alpha \langle 0|\chi_G(\vec{x}, t_{\mathrm{snk}}) J_\mu(\vec{z}, t)\bar{\chi}_G(\vec{0}, t_{\mathrm{src}})|0\rangle] \tag{9}$$

$$= \Lambda^J(q) \times f(t_{\mathrm{src}}, t_{\mathrm{snk}}, t, M_N, E(q), q) + \cdots, \tag{10}$$

where t_{snk} is the sink time slice fixed as $t_{\mathrm{snk}} - t_{\mathrm{src}} = 12$, and $E(q) = \sqrt{M_N^2 + \vec{q}^2}$. The ellipsis denotes the higher excited-state contributions, which can be ignored for long time separations $t_{\mathrm{snk}} \gg t \gg t_{\mathrm{src}}$. The time independent part of $\Lambda^J(q)$ is a matrix element, which is a linear combination of the form factors we seek. The time dependent part of $f(t_{\mathrm{src}}, t_{\mathrm{snk}}, t, M_N, E(q), q)$ includes the kinematical factor and the normalization of the proton operator which we Gaussian smear at both the source and sink. We employ the sequential source method to reduce statistical fluctuations, as in Refs. [20,45]. In the three-point function, initial and final proton states carry $\vec{q}$ and zero momenta, respectively. This is because the spatial momentum should be conserved in the function as in the two-point function.

The time dependence of $f(t_{\mathrm{src}}, t_{\mathrm{snk}}, t, M_N, E(q), q)$ is removed by taking an appropriate ratio of the three- and two-point functions [46]

$$R^{\mathcal{P}_\alpha}_{J_\mu}(q, t) = K \cdot \frac{C^{\mathcal{P}_\alpha}_{J_\mu}(\vec{q}, t)}{C_G(t_{\mathrm{snk}} - t_{\mathrm{src}}, 0)} \left[\frac{C_L(t_{\mathrm{snk}} - t, q) C_G(t - t_{\mathrm{src}}, 0) C_L(t_{\mathrm{snk}} - t_{\mathrm{src}}, 0)}{C_L(t_{\mathrm{snk}} - t, 0) C_G(t - t_{\mathrm{src}}, q) C_L(t_{\mathrm{snk}} - t_{\mathrm{src}}, q)}\right]^{1/2}, \tag{11}$$

where $K = M_N\sqrt{2E(q)(M_N + E(q))}$. The ratio $R^{\mathcal{P}_\alpha}_{J_\mu}$ should display a plateau from which the matrix element we seek is extracted.

For each of the vector or axial-vector currents, we first obtain $\Lambda^J(q)$ in Eq. (10) which is a linear combination of the form factors. For convenience, using the ratio R we define

$$\Lambda^V_4(q, t) = \frac{R^{\mathcal{P}_4}_{V_4}(q, t)}{M_N(M_N + E(q))}, \tag{12}$$

$$\Lambda^V_T(q, t) = -\frac{1}{2}\left(\frac{R^{\mathcal{P}_{53}}_{V_1}(q, t)}{iq_2 M_N} - \frac{R^{\mathcal{P}_{53}}_{V_2}(q, t)}{iq_1 M_N}\right), \tag{13}$$

for the vector current, and

$$\Lambda^A_L(q, t) = \frac{R^{\mathcal{P}_{53}}_{A_3}(q, t)}{M_N(M_N + E(q))}, \tag{14}$$

$$\Lambda^A_T(q, t) = -\frac{1}{2}\left(\frac{R^{\mathcal{P}_{53}}_{A_1}(q, t)}{q_2 q_3} + \frac{R^{\mathcal{P}_{53}}_{A_2}(q, t)}{q_1 q_3}\right), \tag{15}$$

for the axial-vector current. Here we also define $q^2 = 2M_N(E(q) - M_N)$, and $\mathcal{P}_{53} = (1 + \gamma_4)\gamma_5\gamma_3/2$ implies the z-direction is chosen as the polarization direction in our calculation. In the plateau region of $\Lambda^J(q, t)$ we determine the matrix elements of each current, $\Lambda^J(q)$ which has the following relation to the form factors:

$$\Lambda^V_4(q) = F_1(q^2) - \frac{q^2}{4M_N^2} F_2(q^2), \tag{16}$$

$$\Lambda^V_T(q) = F_1(q^2) + F_2(q^2), \tag{17}$$

for the vector current the Sachs form factors Eqs. (2) and (3), and

$$\Lambda^A_L(q) = F_A(q^2) - \frac{q_3^2}{M_N + E(q)} F_P(q^2), \tag{18}$$

$$\Lambda^A_T(q) = M_N F_P(q^2), \tag{19}$$

for the axial-vector current. In the following we use the isovector part of the Dirac and Pauli form factors, $F_{1,2}$, rather than the vector and induced tensor form factors. They are identical through the isospin symmetry except the normalization of the Pauli form factor, $F_2 = 2M_N F_T$. We will see that the signal of these combinations is reasonable in Sec. IV B. Finally, respective form factors are obtained by solving the sets of linear equations, (16) and (17), or (18) and (19), at fixed q^2.

B. Double-source method

We find the ensemble with the lightest quark mass of $m_f = 0.005$ is much noisier than the ones with heavier mass values: it is insufficient and takes an enormous amount of calculation time to obtain reasonable statistical error if we used only a single nucleon source/sink combination per configuration.

Fortunately, the time extent of the lattice, $64 \times a = 7.3$ fm, is very large compared to the inverse of the nucleon mass, $M_N^{-1} = (1.15\ \mathrm{GeV})^{-1} = 0.17$ fm. Hence, we can easily accommodate a pair of source/sink combinations on each configuration without letting them interfere with each other if the sources are separated by 32 units, as shown in Fig. 1. We call this the double-source method.

The three-point functions are calculated with the sequential source method, and the sink operators are placed 12 time slices from their respective sources. The number of the measurements is effectively doubled in this calculation while the cost remains the same as one single source measurement.

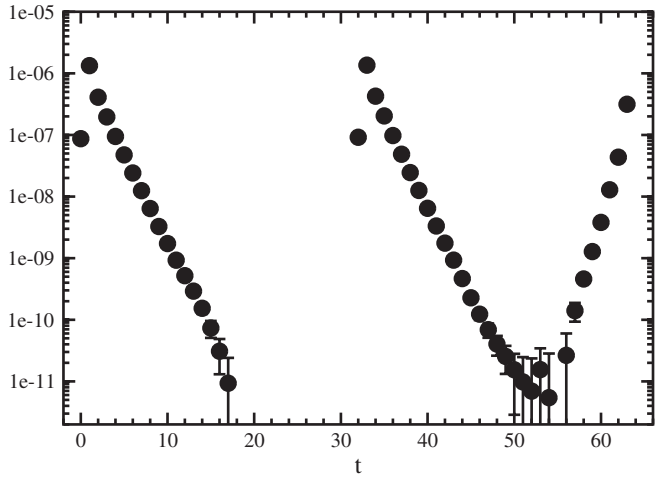

FIG. 1. Two-point function with the double source at $t = (0, 32)$ for $m_f = 0.005$.

III. ENSEMBLES

A. Statistics

The RBC-UKQCD joint (2 + 1)-flavor dynamical DWF coarse ensembles [47] are used for the calculations. These ensembles are generated with Iwasaki gauge action [48] at the coupling $\beta = 2.13$ which corresponds to the lattice cutoff of $a^{-1} = 1.73(3)$ GeV, determined from the Ω^- baryon mass [47].

The dynamical strange and up and down quarks are described by DWF actions with the fifth-dimensional extent of $L_s = 16$ and the domain-wall height of $M_5 = 1.8$. The strange quark mass is set at 0.04 in lattice units and turned out to be about 12% heavier than the physical strange quark, after taking into account the additive correction of the residual mass, $m_{\text{res}} = 0.003$. The degenerate light quark masses in lattice units, 0.005, 0.01, 0.02, and 0.03, correspond to pion masses of about 0.33, 0.42, 0.56, and 0.67 GeV and nucleon masses, 1.15, 1.22, 1.39, and 1.55 GeV.

Two lattice volumes used are $16^3 \times 32$ and $24^3 \times 64$, corresponding to the linear spatial extent of approximately 1.8 and 2.7 fm, respectively. The smaller volume ensembles, calculated only with the heavier three light quark masses, are used for a finite-volume study of the axial charge and form factors discussed in Sec. IV. On the 16^3 ensembles we use 3500 trajectories separated by five trajectories at $m_f = 0.01$ and 0.02, and by 10 at 0.03. The main results are obtained from the larger volume ensembles with the number of the configurations summarized in Table I.

On the larger volume at the heavier three quark masses, we make four measurements on each configuration with the conventional single source method using $t_{\text{src}} = 0$, 16, 32, 48, or 8, 19, 40, 51. At the lightest mass the double-source method is used, and two measurements on each configuration are carried out using the source pairs of (0, 32) and (16, 48), or (8, 40) and (19, 51). We make an additional two measurements on roughly half of the configurations with another source pair. This means that we make four, double-source measurements on almost half of the configurations, while two, double-source measurements are carried out on the remaining configurations. We have checked the independence of these measurements from each other by changing the block size in the jackknife analysis, e.g., treating each source/sink measurement as independent. None of these resulted in a significantly different error estimate: typical results are shown in Fig. 2. Thus in the following we treat the two double-source measurements performed on a single configuration, one with the source pairs of (0, 32) and (16, 48), and the other with the source pairs of (8, 40) and (19, 51), as being independent of each other.

TABLE I. N_{conf}, N_{sep}, and N_{meas} denote the number of gauge configurations, trajectory separation between each measured configuration, and the number of measurements on each configuration, respectively, on $(2.7\ \text{fm})^3$ volume. The table also contains the pion and nucleon mass for each ensemble.

m_f	N_{conf}	N_{sep}	N_{meas}	m_π [GeV]	M_N [GeV]
0.005	932[a]	10	4[b]	0.3294(13)	1.154(7)
0.01	356	10	4	0.4164(12)	1.216(7)
0.02	98	20	4	0.5550(12)	1.381(12)
0.03	106	20	4	0.6681(15)	1.546(12)

[a]The total number of configurations is actually 646. We carry out extra measurements on a subset of these (286 configurations) to improve the statistics using different source positions.
[b]Two measurements with the double-source method give effectively four measurements.

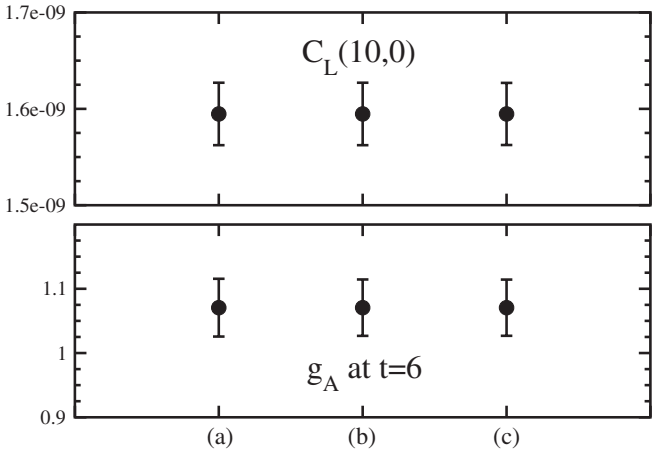

FIG. 2. For $m_f = 0.005$, nucleon propagator $C_L(t, 0)$ at $t = 10$, and axial charge $g_A = C^{\mathcal{P}_{33}}_{A_3}(\vec{0}, t)/C^{\mathcal{P}_4}_{V_4}(\vec{0}, t)$ at $t = 6$ with different jackknife analyses: (a) averaging four data with bin size of 40 trajectories, (b) averaging four data with bin size of 10 trajectories, and (c) treating each measurement as independent with bin size of 10 trajectories.

In the following, in order to reduce possible autocorrelations at the larger volume the measurements are blocked into bins of 40 trajectories each, with 20 trajectories at the smaller volume. The statistical errors are estimated by the jackknife method.

B. Correlation functions

The quark propagator is calculated with an antiperiodic boundary condition in the temporal direction and periodic boundary conditions for the spatial directions. We employ gauge-invariant Gaussian smearing [44] at the source with smearing parameters $(N, \omega) = (100, 7)$, which were chosen after a series of pilot calculations, as described in Ref. [49]. For the calculation of the three-point functions, we use a time separation of 12 time slices between the source and sink operators to reduce effects from excited-state contributions as much as possible.

To obtain the form factors at nonzero q^2, we evaluate the two- and three-point functions, Eqs. (5) and (9), with the four lowest nonzero momenta: $\vec{p} = 2\pi/L \times (0, 0, 1), (0, 1, 1), (1, 1, 1)$, and $(0, 0, 2)$, corresponding to a q^2 range from about 0.2 to 0.75 GeV^2 on the large volume, while on the small volume we use only the smallest two momentum transfers, corresponding to $q^2 \approx 0.4$ and 0.8 GeV^2. All possible permutations of the momentum including the positive and negative directions are taken into account.

There are several choices for the definition of the momentum in the lattice calculation, e.g., $p_i = 2\pi/L \cdot n_i$, $\sin(2\pi a/L \cdot n_i)/a$, or one determined from the measured energy in the two-point function. Figure 3 shows that the three energies with the different momentum definitions reasonably agree with each other. In the following we choose the continuum momentum definition $p_i = 2\pi/L \cdot n_i$, since this simple definition gives smaller statistical error for the energy than the measured one.

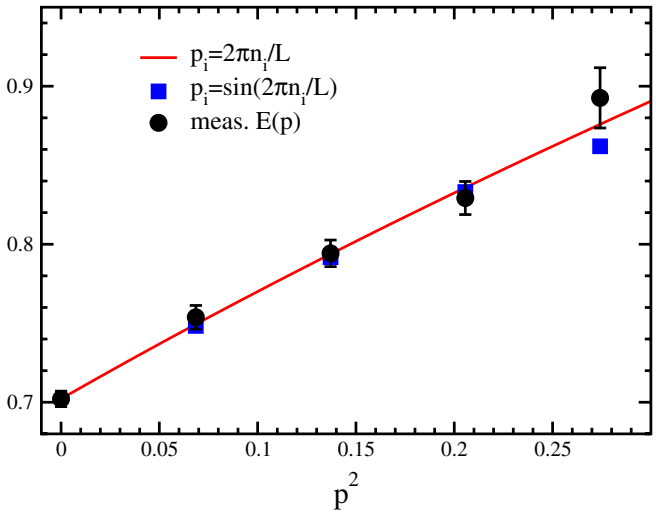

FIG. 3 (color online). Measured nucleon energies in lattice unit at $m_f = 0.01$. Estimated energies by continuum and lattice momenta are also plotted.

C. Systematic errors

There are two important sources of systematic error: finite spatial size of the lattice and excited-state contamination. Chiral-perturbation-theory-inspired analysis of the former for meson observables suggests the dimensionless product, $m_\pi L$, of the calculated pion mass m_π and lattice linear spatial extent L, should be set greater than 4 to ensure that the finite-volume correction is negligible below 1%, and the available lattice calculations seem to support this. While our present parameters satisfy this condition, it should be emphasized that such a practical criterion is not known sufficiently for baryon observables. It is important to check this through the present calculations, and it is indeed an important purpose of this work.

On the other hand, one should adjust the time separation between the nucleon source and sink appropriately so the resultant nucleon observables are free of contamination from excited states. The separation has to be made longer as the quark masses decrease. In our previous study with two dynamical flavors of DWF quarks [2] with a similar lattice cutoff of about 1.7 GeV, we saw systematic differences between observables calculated with the shorter time separation of 10, or about 1.16 fm, and longer 12, or 1.39 fm: the differences amount to about 20%, or 2 standard deviations. This would suggest that at the shorter time separation of about 1.2 fm, the excited-state contamination has not decayed sufficiently to guarantee correct calculations for the ground-state observables [41]. There is, however, a price to pay for the larger time separation as the nucleon correlation function suffers from large statistical noise at large times, especially with light quark masses. Since the hadron masses are much lighter in the present work than we considered previously (the lightest pion mass is 0.33 GeV and nucleon 1.15 GeV) we decided to use the separation of 12 lattice units, or about 1.4 fm.

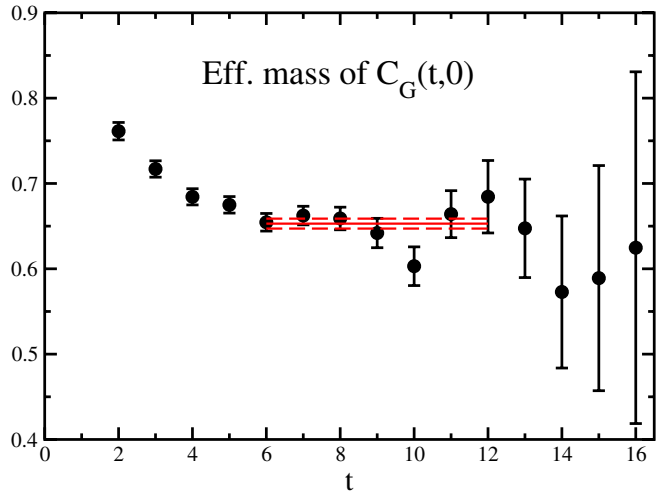

FIG. 4 (color online). Effective mass of the nucleon correlator with Gaussian smearing applied at both source and sink, for quark mass $m_f = 0.005$.

While it is desirable to use a longer separation, it cannot be made too long in practice without losing control of statistical errors. In Fig. 4 we present the nucleon effective mass at the lightest quark mass, $m_f = 0.005$. The nucleon signal begins to decay at $t = 12$, or about 1.4 fm: this is about the longest distance we can choose without losing the signal, and hence about as free of excited-state contamination as we can achieve with the present statistics. As will be shown in detail in this paper, the bare three-point function signals for the form factors for this source-sink separation of $t = 12$ are acceptable. Whether this is a sufficiently long separation between the source and sink to guarantee correct calculations of ground-state observables remains a future problem.

IV. RESULTS

A. Vector and axial charges

Much of the results and discussion in this subsection have appeared in Ref. [39]. We repeat them here for convenience and to lay some of the ground work necessary for discussion of the form-factor results that follow.

At zero momentum transfer the time component of the vector form factor gives the vector charge, $g_V = F_1(0)$. For our calculations at the heaviest three quark masses, we use the four-dimensional local current. As a result, the value of $g_V^{\rm lat}$, measured from the bare $F_1(0)$, deviates from unity and gives the inverse of the renormalization, Z_V, for the local current. At the lightest quark mass, $m_f = 0.005$, we evaluate the vector charge using the point-split conserved vector current [38], $\mathcal{V}_4$ as well. This is to alleviate a problem that arises from the double-source method described in Sec. II B: Conventionally the vector charge is calculated from the ratio of the three-point function with the local vector current to the two-point function with zero momentum, as in Eq. (11); a strong correlation between the denominator and numerator suppresses the statistical error associated with such calculations. This correlation is lost in the double-source calculation and results in larger statistical errors. Fortunately, the three-point functions of the local and conserved currents are highly correlated, even in this method. Therefore we evaluate the vector charge from the ratio of the three-point functions $g_V^{\rm lat} = C_{V_4}^{\mathcal{P}_4}(\vec{0}, t)/C_{\mathcal{V}_4}^{\mathcal{P}_4}(\vec{0}, t)$ at $m_f = 0.005$. Figure 5 shows that the error in this ratio is as small as that coming from the single source calculation at $m_f = 0.01$.

A linear extrapolation to the chiral limit yields an accurate estimate of $g_V^{\rm lat} = 1.3929(17)$, as shown in Fig. 6. This corresponds to $Z_V = 0.7179(9)$ in the chiral limit and agrees well with an independent calculation in the meson sector [47], $Z_A = 0.7161(1)$, up to the discretization error.

The axial charge is calculated from the ratio of the vector and axial-vector form factors $g_A = F_A(0)/F_1(0)$. This ratio gives the renormalized axial charge since the vector and axial currents, V_μ and A_μ, share a common

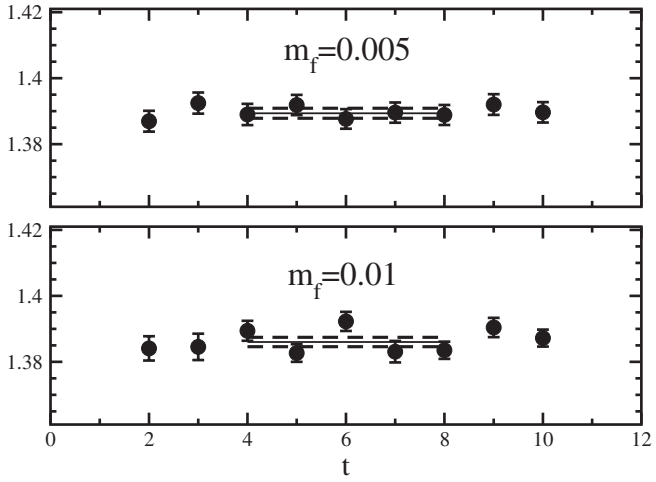

FIG. 5. Plateaus of $g_V^{\rm lat}$ for $m_f = 0.005$ (top) and 0.01 (bottom). Statistical errors are of comparable sizes for the two m_f values despite difference in the methods. Solid lines denote fit results with 1 standard deviation.

renormalization thanks to the good chiral symmetry properties of DWF, up to a small discretization error of $O(a^2)$.

The plateaus of g_A computed on volume $V = (2.7\ \text{fm})^3$ are shown in Fig. 7. We checked that consistent results are obtained by either fitting or averaging over appropriate time slices, $t = 4$–8, and also by fitting the data symmetrized about $t = 6$. The data can be symmetrized because the source and sink operators are identical in the limit of large statistics. We note that the statistics at our lightest mass is the largest we know of for comparable simulation parameters in the literature. Results obtained from the fit using the unsymmetrized data, presented in the figure with 1 standard deviation, are employed in the analysis. These results are compiled in Table II.

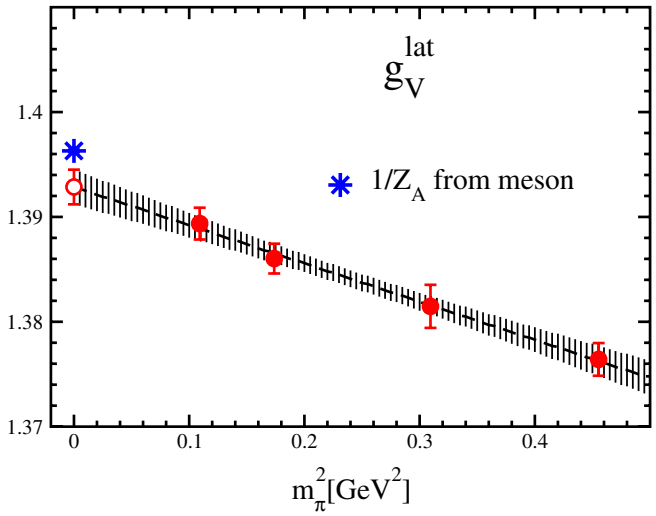

FIG. 6 (color online). $g_V^{\rm lat}$ and $1/Z_A$ obtained from the pion-to-vacuum matrix element of the conserved axial-vector current [47].

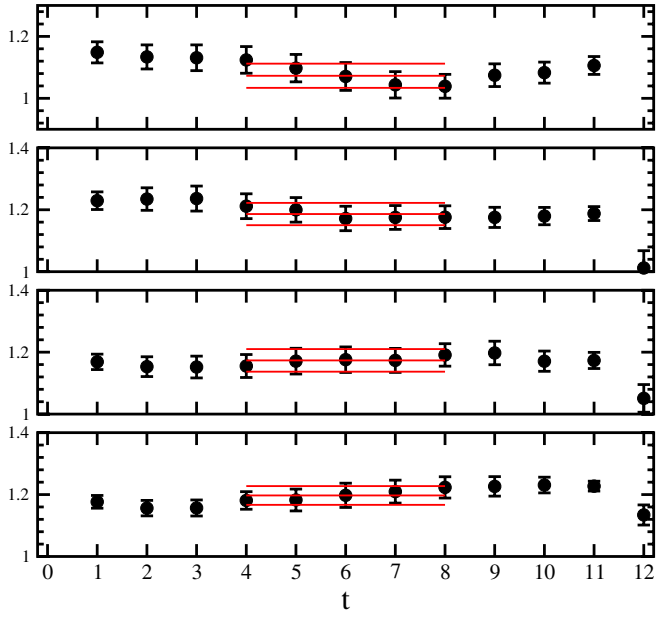

FIG. 7 (color online). Plateaus of g_A. $V = (2.7\ \mathrm{fm})^3$ and $m_f = 0.005$, 0.01, 0.02, and 0.03, from top to bottom.

Figure 8 shows that the $(2.7\ \mathrm{fm})^3$ data are almost independent of the pion mass (squared) except for the lightest point which is about 9% smaller than the others. A set of the results obtained with a smaller volume, $(1.8\ \mathrm{fm})^3$ shows a similar downward behavior, albeit with relatively larger statistical uncertainties. An earlier two-flavor calculation by RBC [2] with spatial volume $(1.9\ \mathrm{fm})^3$ and $1/a = 1.7$ GeV showed a clear downward behavior, but it sets in at heavier pion mass.

We suspect that this pion mass dependence driving g_A away from the experimental value is caused by the finite volume of our calculation. Similar behavior was observed in quenched DWF studies [1,20] and was predicted in a model calculation [50]. However, for pion masses close to our lightest point such a sizable shift is not observed when V is larger than about $(2.4\ \mathrm{fm})^3$, not only in the quenched case, but also the 2 + 1 flavor, mixed-action calculation in [26] and their updated results [29]. Both the results of quenched [1,20] and mixed-action [29] calculations on larger volumes are presented in Fig. 8. On the other hand, our results suggest that a volume of $V = (2.7\ \mathrm{fm})^3$ is not large enough to avoid a significant finite-volume effect on g_A when $m_\pi \leq 0.33$ GeV in dynamical fermion calculations. It is worth noting that the bending of the axial charge comes from only the axial-vector part $F_A(0)$, since

TABLE II. Summary of axial charge, g_A, for both volumes.

m_f	0.005	0.01	0.02	0.03
$(2.7\ \mathrm{fm})^3$	1.073(39)	1.186(36)	1.173(36)	1.197(30)
$(1.8\ \mathrm{fm})^3$	N/A	1.066(72)	1.115(58)	1.149(32)

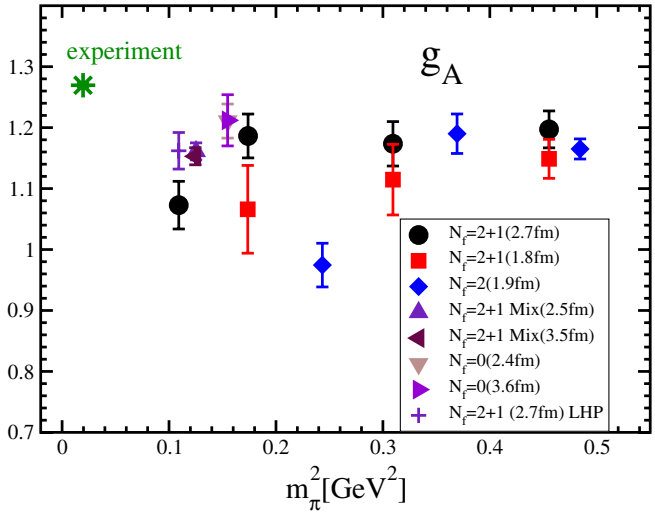

FIG. 8 (color online). Axial charge g_A together with two-flavor [2] and quenched [1,20] DWF, and mixed-action [26,29] calculations. Recent $N_f = 2 + 1$ DWF by LHP [29] is also plotted.

the vector part $F_1(0)$ does not have such a pion mass dependence (see Fig. 6).

In order to more directly compare the various results, we plot g_A against the dimensionless quantity, $m_\pi L$, in the top panel of Fig. 9. We find that the 2 + 1 flavor results on both volumes reasonably collapse onto a single curve that monotonically increases with $m_\pi L$; in other words, they exhibit scaling in this variable. The two-flavor results [2] display a similar behavior which is also evident in dynamical two-flavor (improved) Wilson fermion calculations as shown in the middle panel [24,27,51] for the unitary points $\kappa_{\mathrm{sea}} = \kappa_{\mathrm{val}}$, with various volumes (0.95–2.0 fm)^3, pion masses 0.38–1.18 GeV, and gauge couplings. While the trend is similar in the quenched DWF case [1,20] with pion masses in the range 0.39–0.86 GeV and $1/a = 1.3$ GeV (see bottom panel), the scaling is violated for the point with smallest $m_\pi L$ on $V = (2.4\ \mathrm{fm})^3$. The lightest point does not follow the $(1.8\ \mathrm{fm})^3$ data: they differ by 2.5 standard deviations (σ) at $m_\pi L \sim 5$, suggesting that there are non-universal terms that depend separately on m_π and V. In particular, this effect may be due to the presence of a quenched chiral log [52]. From Ref. [52], the size of the effect at this mass can readily explain the discrepancy observed with the dynamical $m_\pi L$ scaling. Note, at this mass, but going to $V = (3.6\ \mathrm{fm})^3$, no finite-volume effect is detected in the quenched case as can be seen in Fig. 8.

The mixed-action, 2 + 1 flavor result with a similar volume [26,29], is denoted by the left triangle in the top panel. We plot their recent result at our lightest point [29]. At heavy pion masses the results are statistically consistent with our larger volume data and essentially independent of $m_\pi L$. At $m_\pi L \sim 4.5$ the mixed-action result, however, is larger than ours by (a combined) 2.1σ and lies between our lightest result and the quenched DWF result with $(2.4\ \mathrm{fm})^3$ volume [20] (the up triangle in the figure).

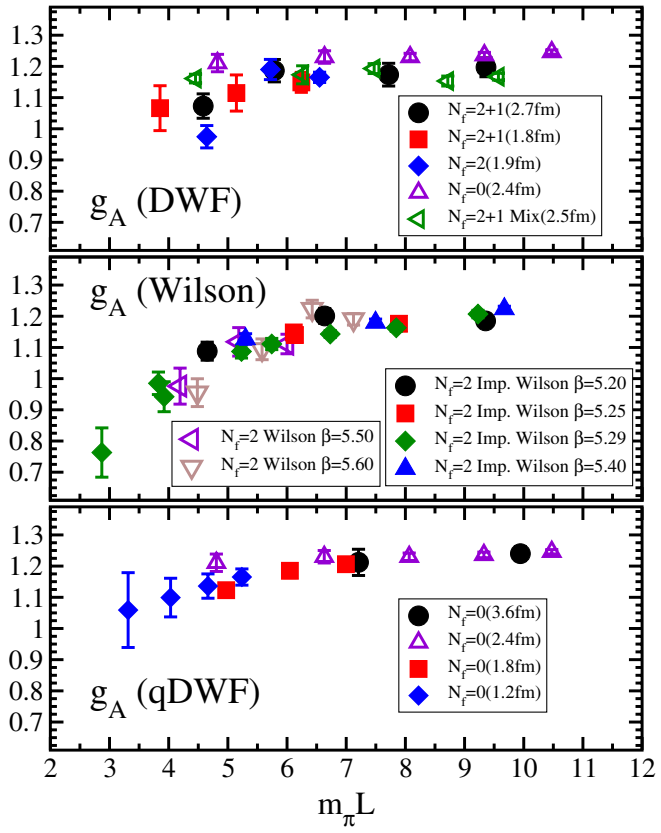

FIG. 9 (color online). $m_\pi L$ scaling of the axial charge. Top, middle, and bottom panels are dynamical DWF, dynamical Wilson, and quenched DWF results [1,20], respectively. In the top panel the circle, square, and diamond denote $2+1$ flavor larger, smaller volumes, and 2 flavor data [2], respectively, and the open up and left triangles denote quenched [20] and mixed-action [26,29] data, respectively. In the middle panel closed symbols denote dynamical improved-Wilson fermions [24] and open symbols are dynamical Wilson fermion [27,51]. In the bottom panel, the open triangle is the same as in the top panel.

A possible explanation of the differences is that it is simply a dynamical fermion effect as discussed in Ref. [39]. While the mixed-action result at $m_\pi L \sim 4.5$ has come down from higher value with larger error (the previous result was consistent with the quenched result at the similar $m_\pi L$), the explanation using the systematic error [53,54] of the partially quenched effect of the mixed-action results might be valid in the present data. If the sea quark is effectively heavy, a mixed-action calculation will be closer to the quenched case. Mixed-action chiral perturbation theory reveals the presence of partially quenched logs whose size is consistent with the observed effect [55,56], as in the quenched theory. We should note that the preliminary result obtained by LHP [29] at the same simulation parameter as our lightest point appears inconsistent with our result (see Fig. 8). We will discuss the difference later in this section.

For the chiral extrapolation of g_A, we attempt to include the finite-volume effect in our data. While the pion mass dependence of g_A, including the finite-volume effect, has been investigated in the small scale expansion (SSE) scheme of heavy baryon chiral perturbation theory (HBChPT) [24], the size of the finite-volume effect on $V = (2.7\ \mathrm{fm})^3$ predicted in SSE is less than 1% in our pion mass region. The correction is much too small to account for the observed finite-volume effect in our data. This suggests that the finite-volume effect in HBChPT, which is estimated by replacing all loop integrals by summations, is not the leading finite-volume effect in g_A, as in the ε' [57] and ε [58] regimes. We also note that our attempts to fit the mass dependence of the data to HBChPT failed, which is likely due to the heavier quark mass points being beyond the radius of convergence of ChPT [2,47,59].

Instead of the SSE formula, we assume the following simple fit form, including the finite-volume effect in a way that respects the scaling observed in the data:

$$A + Bm_\pi^2 + Cf_V(m_\pi L), \tag{20}$$

with $f_V(x) = \mathrm{e}^{-x}$, and where A, B, and C are fit parameters. The third term corresponds to the observed finite-volume effect, taken as a function of $m_\pi L$ only, and vanishes rapidly towards the infinite volume limit, $L \to \infty$, at fixed pion mass. The same $m_\pi L$ dependence appears in one of the finite-volume effect contributions in Ref. [60]. We note that this simple form is used to estimate the finite-volume effects in the data but *not* the value of g_A in the chiral limit at fixed L. In the end, we choose this simplest form, in part, because the fit result at the physical point is not sensitive to the particular choice of $f_V(x)$, as discussed below.

In Fig. 10 we see that the $2+1$ flavor data are described very well by this simple fit (χ^2/d.o.f. $= 0.57$), using data computed on both volumes simultaneously. The $L \to \infty$ extrapolation (solid line) in turn allows an extrapolation to

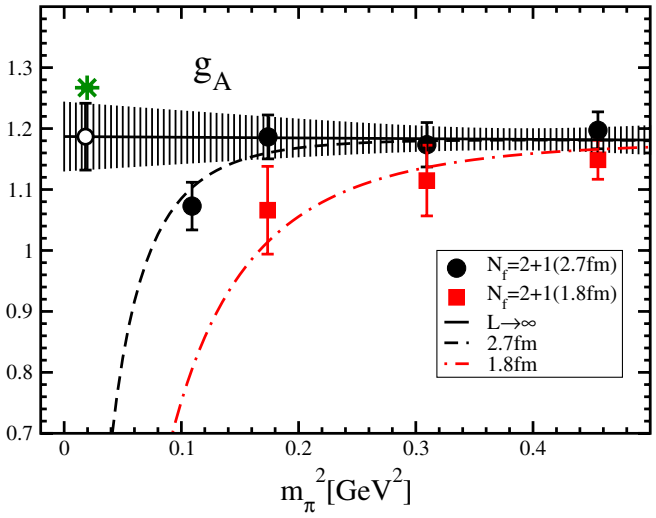

FIG. 10 (color online). Chiral and infinite volume extrapolation of g_A with a finite-volume effect $f_V = \mathrm{e}^{-x}$ in Eq. (20). The fit is carried out with data on both the volumes, simultaneously.

TABLE III. Fit results of g_A, together with the extrapolated result at $m_\pi^{\rm phys} = 135$ MeV. In the last row, the linear fit result using only the three heavier points at $V = (2.7\ {\rm fm})^3$ is presented.

f_V	A	B	C	χ^2/d.o.f.	$m_\pi^{\rm phys}$
$e^{-m_\pi L}$	1.187(57)	−0.12(14)	−8.1(3.9)	0.60	1.187(55)
$(m_\pi L)^{-3}$	1.226(70)	−0.05(15)	−11.3(5.2)	0.47	1.225(67)
$m_\pi^2 e^{-m_\pi L}/\sqrt{m_\pi L}$	1.148(46)	−0.09(12)	−75(41)	0.80	1.150(44)
N/A	1.172(58)	0.05(1.7)	—	0.17	1.173(55)

the physical pion mass ($m_\pi = 135$ MeV), $g_A = 1.19(6)(4)$, where the first error is statistical. The second error is an estimate of the systematic error determined by comparing this result with that from fits using different choices of $f_V(x)$, e.g., the full form in [60], x^{-3}, and $m_\pi^2 {\rm e}^{-x}/x^{1/2}$. The latter is similar to HBChPT when $m_\pi L \gg 1$ [24,61,62]. The results of some of the fit forms are summarized in Table III. The extrapolated value is not sensitive to the choice of f_V and is consistent with a linear fit to the three heaviest points on the larger volume, $g_A = 1.17(6)$. The present data are insufficient to determine the detailed form of f_V, but do allow a reasonable estimate of the finite-volume effect.

We also fit our data, with and without the f_V term, to the two-loop formula from HBChPT [59] and find that the extrapolated result is less than 1 and that the fits are generally unstable. This is due to the many unknown low energy constants which cannot be determined accurately from only four data points, even if some of them are fixed. More importantly, though the two-loop formula extends the range of applicability of the chiral expansion, it is still only large enough to include our lightest point, as demonstrated in Ref. [59]. The systematic error arising from the difference of the renormalization constants for A_μ and V_μ is much smaller than the quoted systematic error. From the fit result with $f_V(x) = {\rm e}^{-x}$, we estimate that if one aims to keep finite-volume effects at or below 1%, then for $m_\pi = 0.33$ GeV, spatial sizes of 3.5–4.1 fm ($m_\pi L \approx 5.9$–6.9) are necessary.

As mentioned, our lightest result on $(2.7\ {\rm fm})^3$ differs from the preliminary findings from LHP [29] shown in Fig. 8 by 1.8σ. These calculations are carried out with the same parameters except for the operator smearing and the time separation between the source and sink operators, $\Delta t = t_{\rm sink} - t_{\rm src}$. So, while it is possible that this difference is simply due to the limited statistics in the preliminary result in [29], there is the possibility that this difference is due to a systematic error stemming from contaminations of higher excited states. These contaminations will be negligible when the time separation of the two nucleon operators in the three-point function, Eq. (9), is large enough. The large separation, however, causes the statistical error of the three-point function to increase. Thus, we employ a time separation of $\Delta t = 12$, as described in Sec. II, while LHP uses $\Delta t = 9$. While further investigation of this difference is desirable, it is beyond the scope of this paper.

Although there may be a systematic difference between our result and the result of LHP at the lightest quark mass on the $(2.7\ {\rm fm})^3$ lattice, all recent results [29,63] (before chiral extrapolation) with dynamical quarks are about 10% smaller than the experimental value. In order to make a precise test of (lattice) QCD with the axial charge, further study of the systematic errors as the quark mass is decreased towards the physical point is required on large volumes.

B. Form factors of the vector current

In this subsection we discuss the isovector part of the Dirac and Pauli form factors, $F_1(q^2)$ and $F_2(q^2)$. In Fig. 11 we present the ratios of the three- and two-point functions,

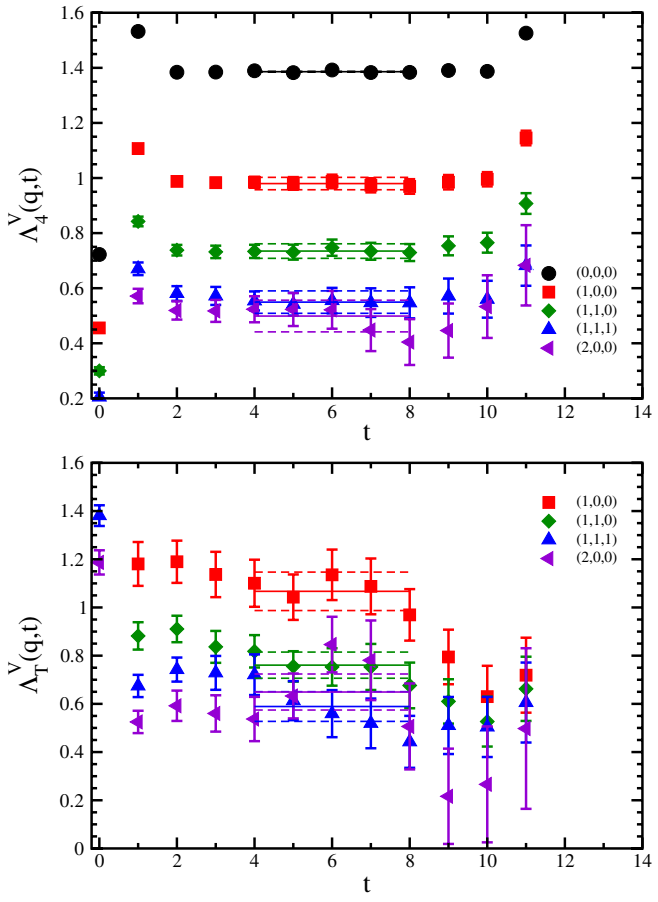

FIG. 11 (color online). Ratios of two- and three-point functions of the vector current, Λ_4^V and Λ_T^V, at $m_f = 0.01$.

TABLE IV. Form factors of vector, axial-vector currents on $(2.7\ \mathrm{fm})^3$. All form factors are renormalized.

m_f	q^2 [GeV^2]	$F_1(q^2)$	$F_2(q^2)$	$F_A(q^2)$	$2M_N F_P(q^2)$
0.005	0.0	1.0000(11)	N/A	1.073(39)	N/A
	0.198	0.785(19)	2.20(13)	0.959(34)	13.32(91)
	0.383	0.622(22)	1.716(97)	0.892(39)	7.42(51)
	0.557	0.505(28)	1.40(10)	0.754(41)	5.27(42)
	0.723	0.516(53)	1.36(16)	0.792(65)	4.71(53)
0.01	0.0	1.0000(10)	N/A	1.186(33)	N/A
	0.199	0.787(17)	2.38(15)	0.994(37)	13.00(90)
	0.385	0.641(22)	1.71(12)	0.854(37)	7.48(44)
	0.562	0.524(31)	1.34(11)	0.719(39)	5.01(42)
	0.731	0.506(49)	1.19(13)	0.701(57)	3.95(46)
0.02	0.0	1.0000(15)	N/A	1.174(37)	N/A
	0.200	0.805(20)	2.40(15)	1.005(33)	12.3(1.2)
	0.390	0.686(32)	2.08(13)	0.890(38)	9.04(73)
	0.573	0.599(49)	1.80(13)	0.839(48)	7.06(70)
	0.748	0.443(37)	1.31(14)	0.668(47)	3.84(59)
0.03	0.0	1.0000(11)	N/A	1.196(30)	N/A
	0.201	0.8302(99)	2.79(12)	1.038(28)	12.74(88)
	0.394	0.700(15)	2.302(92)	0.912(32)	9.68(62)
	0.580	0.595(22)	2.00(12)	0.838(40)	6.81(61)
	0.760	0.500(31)	1.54(15)	0.704(50)	4.55(73)

Λ_4^V and Λ_T^V defined in Eqs. (12) and (13), at the quark mass $m_f = 0.01$ for each momentum transfer. We find excellent plateaus in the middle time region between the nucleon source and sink operators at $t = 0$ and 12 for the smaller momenta, while the plateau at $\vec{q} \propto (2, 0, 0)$ is not as well behaved and has a larger error. This is interpreted as simply a statistical fluctuation. In order to remove this wiggle, we would need more statistics at this momentum. To determine the values of the ratios, we perform a constant fit in the time interval, $t = 4$–8, for all momentum combinations.

The form factors are obtained by solving the linear equations (16) and (17),

$$F_1(q^2) = \frac{\Lambda_4^V(q) + \tau \Lambda_T^V(q)}{1 + \tau}, \quad \text{for all } q, \tag{21}$$

$$F_2(q^2) = \frac{\Lambda_T^V(q) - \Lambda_4^V(q)}{1 + \tau}, \quad \text{for } q \neq 0, \tag{22}$$

where $\tau = q^2/(4M_N^2)$. All the values of the two form factors are shown in Table IV.

1. Dirac form factor $F_1(q^2)$

Let us now turn our attention to the momentum dependence of the Dirac form factor. In Fig. 12 we present the form factor at each quark mass normalized by the respective values at zero momentum transfer.

Phenomenologically the form factor is described by the conventional dipole form,

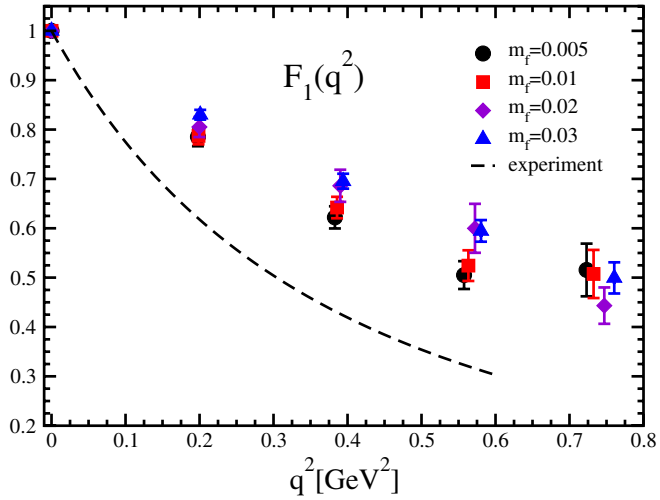

FIG. 12 (color online). The Dirac form factor, $F_1(q^2)$, normalized to unity at $q^2 = 0$.

$$F_1(q^2) = \frac{1}{(1 + q^2/M_1^2)^2}, \tag{23}$$

where M_1 is the dipole mass for this form factor, and fits to experimental data give $M_1 = 0.857(8)$ GeV [12]. In order to test the dipole form using our lattice results, for convenience we define an effective dipole mass

$$M_1^{\mathrm{eff}} = \sqrt{\frac{q^2}{\sqrt{1/F_1(q^2)} - 1}}. \tag{24}$$

Figure 13 shows that the effective dipole mass at $m_f = 0.01$ is almost flat against q^2. This means that the form factor is well explained by the dipole form Eq. (23) in the

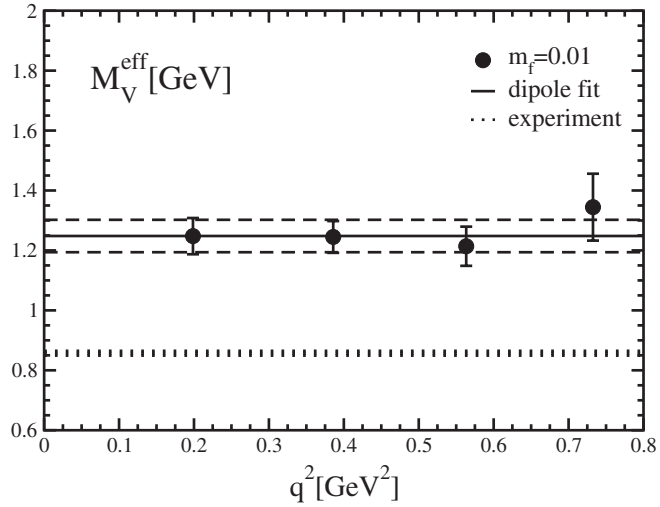

FIG. 13. Effective dipole mass M_1^{eff} for $F_1(q^2)$ at $m_f = 0.01$ together with the experimental result [12,23]. The result of the dipole fit (solid line) with 1 standard deviation (dashed line) is also presented.

TABLE V. Dirac and Pauli rms radii $\langle r_1^2\rangle^{1/2}$, $\langle r_2^2\rangle^{1/2}$, and anomalous magnetic moment $F_2(0) = \mu_p - \mu_n - 1$. The linear fit results at $m_\pi^{\rm phys} = 135$ MeV are also presented.

m_f	0.005	0.01	0.02	0.03	$m_\pi^{\rm phys}$
$\langle r_1^2\rangle^{1/2}$ [fm]	0.564(23)	0.548(24)	0.520(31)	0.485(16)	0.584(23)
$\langle r_2^2\rangle^{1/2}$ [fm]	0.578(60)	0.690(61)	0.536(21)	0.537(38)	0.636(57)
$F_2(0)$	2.82(26)	3.40(35)	3.11(21)	3.55(19)	2.75(28)

q^2 region where we measure. The figure also shows that the effective mass is consistent with the dipole fit result as expected.

We estimate the Dirac root-mean-squared (rms) radius from the dipole mass obtained by the fit as

$$\langle r_1^2\rangle^{1/2} = \frac{\sqrt{12}}{M_1}, \tag{25}$$

whose results are presented in Table V. Figure 15 shows the pion mass dependence of our results for the rms radius. Here we also compare with other lattice calculations and the experimental value. Our results show a near-linear dependence in the pion mass squared which is quite different from the axial charge in Sec. IV A. This suggests that the Dirac form factor is less sensitive to the finite-volume effect than g_A, and this is confirmed by an analysis of our results obtained on a smaller volume $(1.8\ \text{fm})^3$, shown in Fig. 14. The smaller volume results are summarized in Table VI. Our results can be fit linearly and extrapolated to a value 27% smaller than experiment, 0.797(4) fm. Other lattice calculations [1,2,22,23,25] show similar trends. The recent results of the mixed-action calculation [29] are also statistically consistent with our data and fit line.

This quantity is expected to logarithmically diverge in HBChPT [64–66] at the chiral limit: such a behavior will help in bringing our present extrapolated results closer to experiment. However, our results at $m_\pi > 0.33$ GeV fail to reveal such a logarithmic divergence. A naive determination of the HBChPT parameters at the physical point give the logarithmic contribution shown in Fig. 15 by the solid line. Future work will require simulations to be performed at lighter quark masses, e.g., $m_\pi < 0.2$ GeV, if such loga-

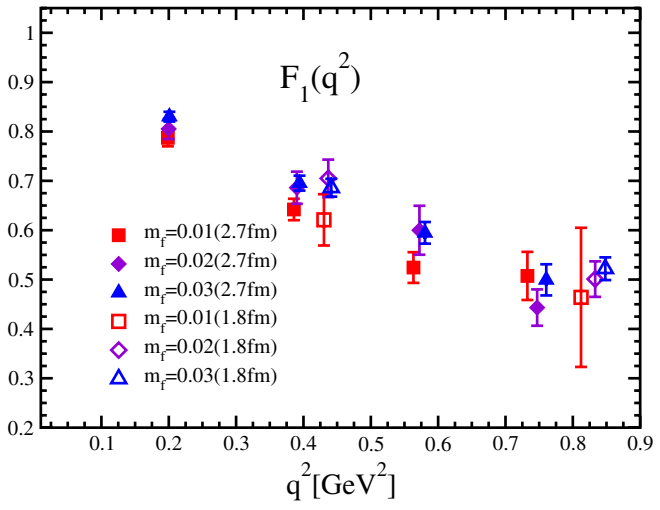

FIG. 14 (color online). Comparison of F_1 with larger and smaller volumes denoted by closed and open symbols, respectively, at each quark mass.

TABLE VI. Form factors of vector, axial-vector currents on $(1.8\ \text{fm})^3$. All form factors are renormalized.

m_f	q^2 [GeV^2]	$F_1(q^2)$	$F_2(q^2)$	$F_A(q^2)$	$2M_N F_P(q^2)$
0.01	0.0	1.000(27)	N/A	1.066(72)	N/A
	0.430	0.621(52)	1.42(23)	0.580(93)	3.2(1.4)
	0.812	0.46(14)	0.89(50)	0.380(70)	1.83(68)
0.02	0.0	1.000(14)	N/A	1.115(58)	N/A
	0.437	0.705(38)	2.03(17)	0.749(49)	6.16(97)
	0.833	0.501(36)	1.14(14)	0.504(47)	2.70(38)
0.03	0.0	1.0000(6)	N/A	1.149(32)	N/A
	0.441	0.686(18)	1.91(10)	0.787(29)	6.56(70)
	0.848	0.522(23)	1.258(70)	0.574(30)	3.48(30)

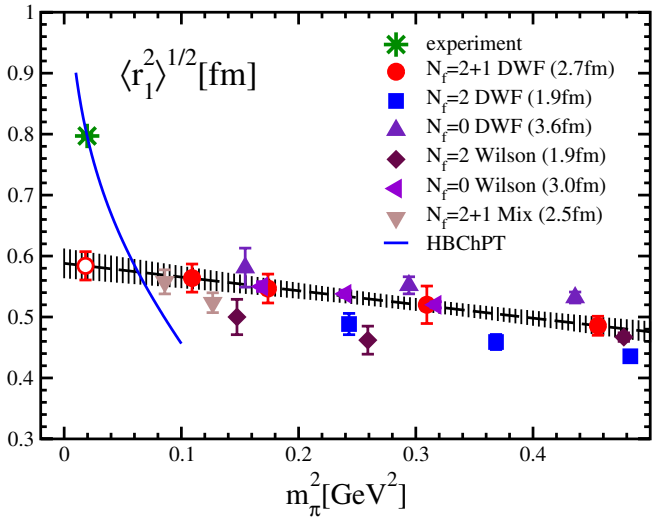

FIG. 15 (color online). Dirac rms radius $\langle r_1^2\rangle^{1/2}$ determined from a dipole fit. The dashed line with error band represents a linear extrapolation of our results. Square, up triangle, diamond, left triangle, and down triangle denote two-flavor [2] and quenched DWF [1], two-flavor and quenched Wilson [23], and mixed-action [29] calculations, respectively. A prediction from HBChPT with the experimental result [12,23] is also plotted.

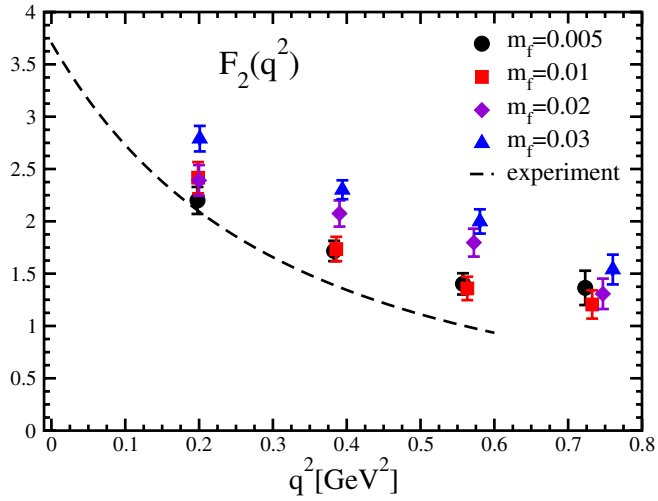

FIG. 16 (color online). The Pauli form factor, $F_2(q^2)$, renormalized by $Z_V = 1/F_1(0)$. The dashed curve is a fit to experimental data.

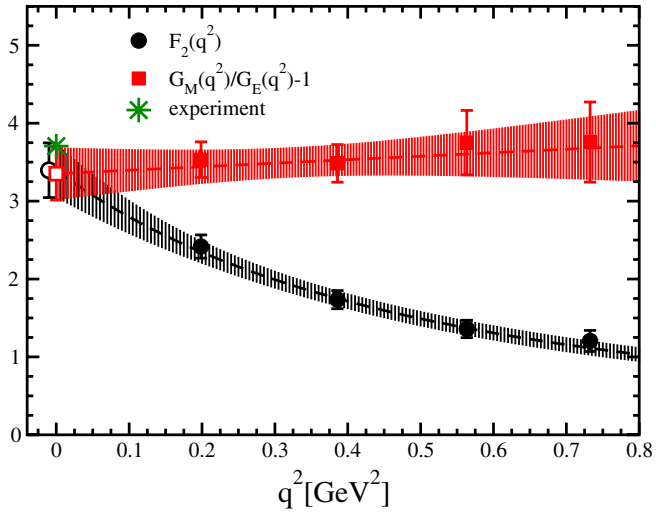

FIG. 17 (color online). Dipole fit with $F_2(q^2)$ and linear fit with the ratio of electric and magnetic form factors $G_M(q^2)/G_E(q^2) - 1$ at $m_f = 0.01$. The result of the ratio at $q^2 = 0$ is shifted to the minus direction in the x-axis.

rithmic effects are to be seen in lattice results of the Dirac radius.

2. *Pauli form factor* $F_2(q^2)$

Figure 16 shows the momentum-transfer dependence of our results for the Pauli form factor at each quark mass. These values are tabulated in Table IV. The form factor is renormalized by $F_1(0)$.

This form factor can also be described by the conventional dipole form,

$$F_2(q^2) = \frac{F_2(0)}{(1 + q^2/M_2^2)^2}, \tag{26}$$

with $M_2 = 0.78(2)$ GeV and $F_2(0) = 3.705\,89$ extracted from fits to experimental data. In contrast to the Dirac form factor, there are two parameters, the overall strength $F_2(0)$ and the dipole mass M_2: the former gives the isovector part of the anomalous magnetic moment, $\mu_p - \mu_n - 1$, and the latter the Pauli mean-squared radius, $\langle r_2^2 \rangle = 12/M_2^2$, as in the Dirac case. We fit the form factor with these two parameters.

To check reliability of the dipole fit, we measure the ratio of the Sachs electric and magnetic form factors, Eqs. (2) and (3),

$$\frac{G_M(q^2)}{G_E(q^2)} = \frac{\Lambda_T^V(q)}{\Lambda_4^V(q)}, \tag{27}$$

which exhibits a mild q^2 dependence [1,49]. At zero momentum transfer, we obtain $1 + F_2(0)$ from the ratio. Figure 17 shows that the result for $G_E(q^2)/G_M(q^2) - 1$ at $q^2 = 0$, obtained via a linear fit in q^2, is consistent with the determination from a dipole fit of $F_2(q^2)$.

In Fig. 18 we present the anomalous magnetic moment of the nucleon, determined by the dipole fit presented in Table V, together with some other lattice QCD calculations and the experimental value. Our present results slightly decrease with the pion mass, in agreement with previous lattice calculations [1,23]. They extrapolate well linearly in the pion mass squared and result in a value 26% smaller than the experiment. This result at the physical pion mass is consistent with those of previous calculations [1,19] using a linear fit.

We present in Fig. 19 the result of the Pauli rms radius. These results are obtained from a dipole fit and summarized in Table V. Some other lattice QCD calculations [1,23] are also plotted in the figure for comparison. We

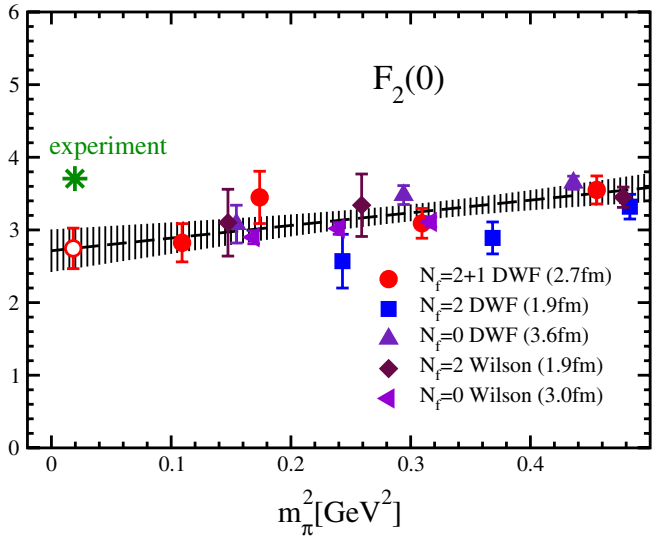

FIG. 18 (color online). Same as Fig. 15 except anomalous magnetic moment, $F_2(0) = \mu_p - \mu_n - 1$, determined from the dipole fit. The experimental result [12] is also shown.

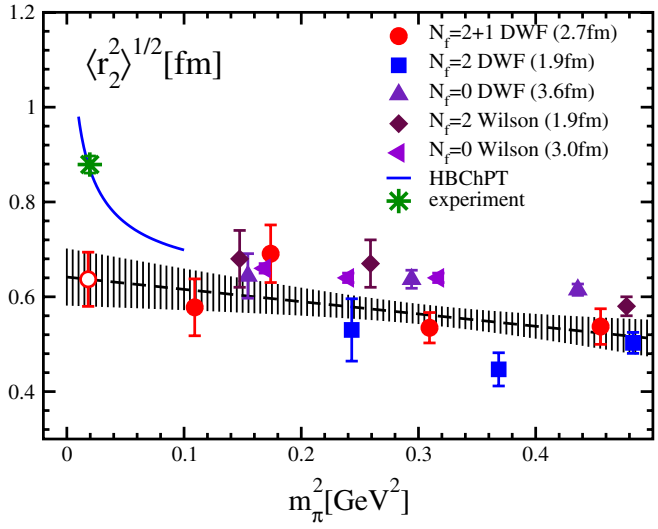

FIG. 19 (color online). Same as Fig. 15 except Pauli rms radius $\langle r_2^2 \rangle^{1/2}$ determined from the dipole fit. Prediction of HBChPT with the experimental result [12,23], and fit result with HBChPT prediction (dash-dot line) are also plotted. The striped symbol is shifted to the minus direction in the x-axis.

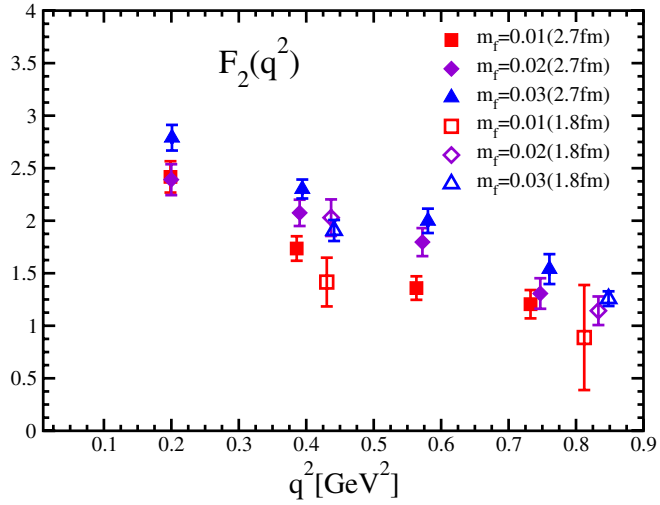

FIG. 20 (color online). Comparison of F_2 with larger and smaller volumes denoted by closed and open symbols, respectively, at each quark mass.

find the lightest point to be slightly smaller than the results at the other quark masses, albeit with a large error. Thus, we consider this pion mass dependence is due to statistics, not a finite-volume effect as in the axial charge, and this is confirmed by our results from the smaller volume simulations in Fig. 20. The results are reasonably fitted by a linear function of the pion mass squared, and we obtain $\langle r_2^2 \rangle^{1/2} = 0.64(6)$ fm at the physical pion mass. This result again is 27% smaller than the experimental value, 0.88(2) fm.

Here again the quantity is expected to diverge as $1/\sqrt{m_\pi}$ in the chiral limit in HBChPT [64–66], however our results do not indicate such divergence. In contrast to the Dirac radius case, perhaps because of the larger statistical errors, HBChPT can simultaneously fit the experiment and our data. The fit inspired by a prediction [64],

$$\frac{A}{\sqrt{m_\pi}}\left(1 + Bm_\pi + Cm_\pi \log\left(\frac{m_\pi}{\mu}\right)\right), \tag{28}$$

where A, B, and C are free parameters ($A = \sqrt{g_A^2 M_N/8\pi F_\pi^2 F_2(0)}$ in HBChPT), μ is the scale and fixed to 1 GeV for simplicity, gives a larger χ^2/d.o.f.(degrees of freedom) = 3.4. We cannot obtain a reasonable χ^2/d.o.f. without fixing the coefficient A using the experimental values. We need further light quark mass calculation with better statistics to test the prediction in the lattice QCD calculation.

C. Form factors of the axial-vector current

In this subsection we show the form factors obtained from the axial-vector currents, $F_A(q^2)$ and $F_P(q^2)$. They are extracted from the ratios of three- and two-point functions defined in Eqs. (14) and (15). Figure 21 shows that the typical plateaus of the ratios with the A_3 component of the current at $m_f = 0.01$ are reasonably flat in the middle time region between the source and sink operators. We plot the ratios $\Lambda_L^A(q_3 = 0, t)$ and $\Lambda_L^A(q_3 \neq 0, t)$ separately, since $\Lambda_L^A(q_3 \neq 0, t)$ contains both form factors, while $\Lambda_L^A(q_3 = 0, t)$ contains only $F_A(q^2)$. It is worth noting that there is no $\Lambda_L^A(q_3 = 0, t)$ in the case of $\vec{q} \propto (1, 1, 1)$. $\Lambda_T^A(q, t)$ has a slope in the range $t = 1$–8 with large statistical errors as shown in the bottom panel of Fig. 21. We consider the slope to be caused by poor statistics in the data. The values of the matrix elements for all the ratios are determined by constant fits with the range of $t = 4$–8.

Using the relations Eqs. (18) and (19), the two form factors are determined through the following equations which depend on the spatial momentum transfer in the three-point function:

$$F_A(q^2) = \begin{cases} \Lambda_L^A(q_3 = 0) & \text{for } n = 0, 1, 2, 4 \\ \Lambda_L^A(q_3 \neq 0) + \frac{q_3^2}{M_N(M_N + E(q))}\Lambda_T^A(q) & \text{for } n = 3 \end{cases}, \tag{29}$$

$$F_P(q^2) = \begin{cases} \Lambda_T^A(q)/M_N & \text{for } n = 2, 3 \\ \frac{M_N + E(q)}{q_3^2}(\Lambda_L^A(q_3 = 0) - \Lambda_L^A(q_3 \neq 0)) & \text{for } n = 1, 4 \end{cases}, \tag{30}$$

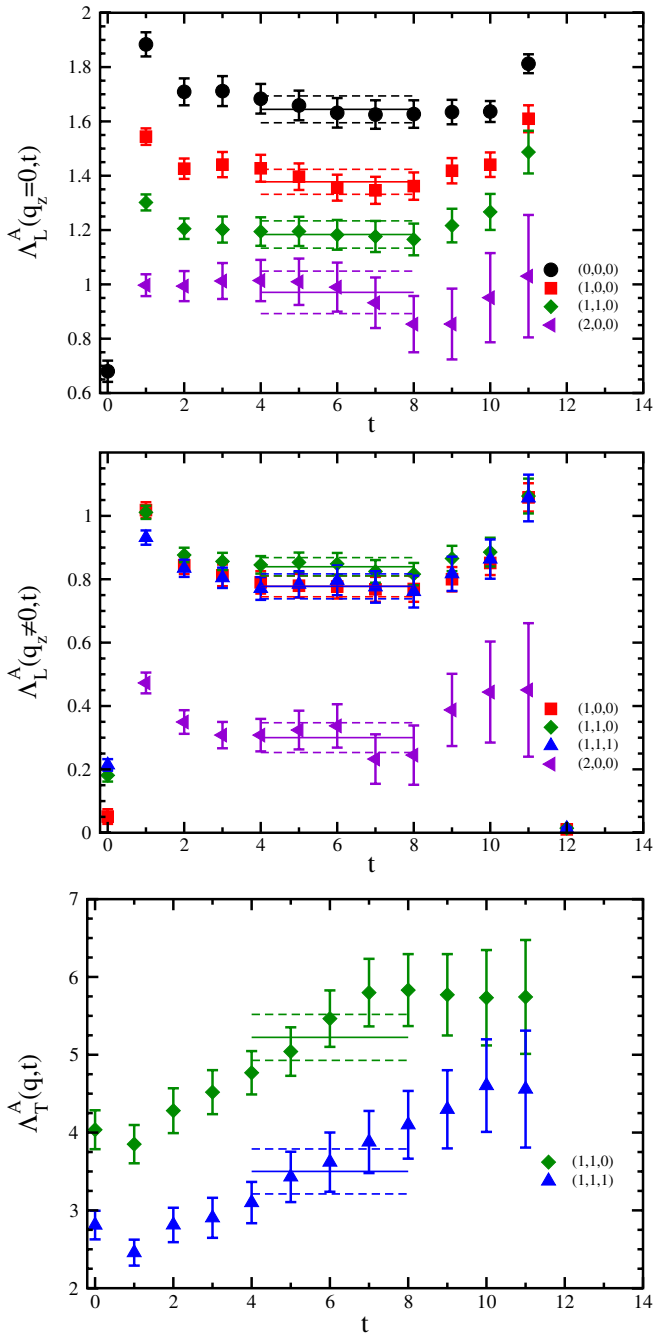

FIG. 21 (color online). Ratios of two- and three-point functions for the axial-vector current, $\Lambda_L^A(q_3 = 0, t)$, $\Lambda_L^A(q_3 \neq 0, t)$, and $\Lambda_T^A(q, t)$ at $m_f = 0.01$.

where $n = \vec{q}^2 \cdot (L/2\pi)^2$. The results for the two form factors are summarized in Table IV.

1. Axial-vector form factor $F_A(q^2)$

Figure 22 shows the axial-vector form factor at each quark mass, which is renormalized by the Dirac form factor at zero momentum transfer, $Z_V = 1/F_1(0)$. This renormalization is valid due to the good chiral properties

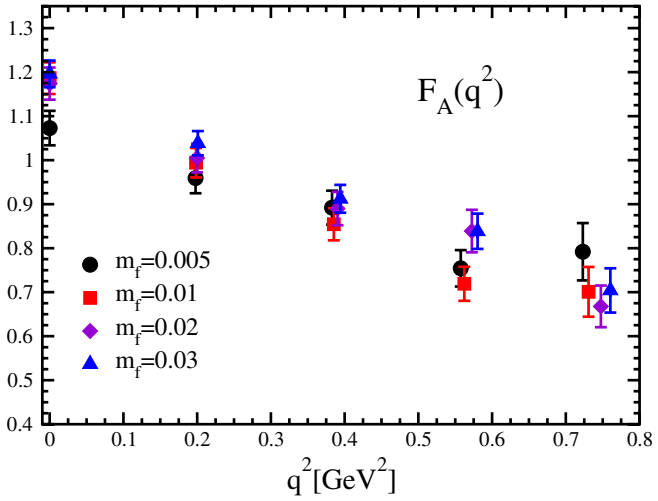

FIG. 22 (color online). The axial-vector form factor, $F_A(q^2)$, renormalized by $Z_V = 1/F_1(0)$.

of DWF. At zero momentum transfer, the result at $m_f = 0.005$ is smaller than the other masses which corresponds to the bending of g_A discussed in Sec. IVA. Furthermore, the q^2 dependence of the results at the lightest quark mass is milder than the other masses.

In the following we focus only on the momentum-transfer dependence of the axial-vector form factor: We normalize the form factor by its value at zero momentum transfer, respectively, for each quark mass. Figure 23 shows the results after these normalizations, $F_A(q^2)/F_A(0)$. For the heavier three masses, the results tend to decrease with quark mass while the dependence is opposite for the lightest mass. Similar to the vector-current form factors, the experimental axial-vector form factor is also traditionally considered to be fitted well by

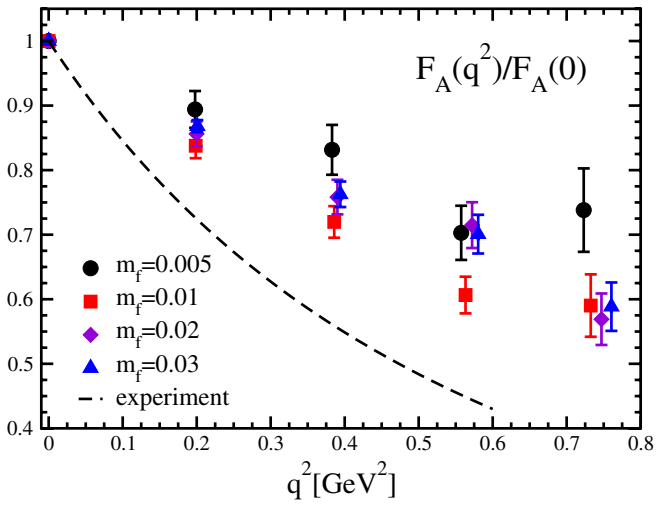

FIG. 23 (color online). The axial-vector form factor, $F_A(q^2)$, normalized at $q^2 = 0$. The dashed line denotes a fit to experimental data.

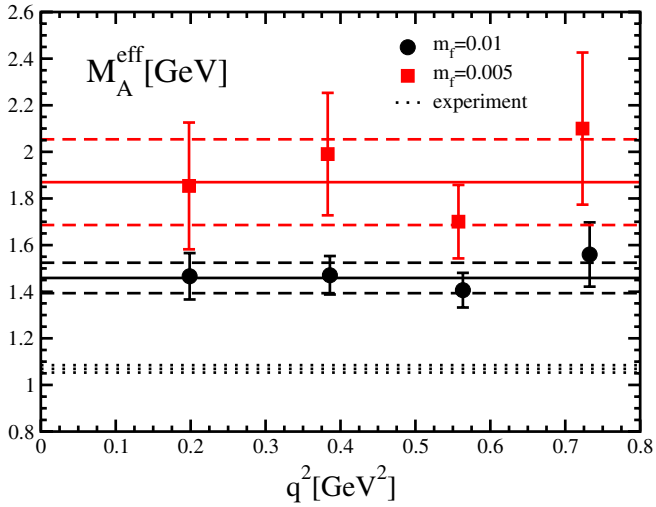

FIG. 24 (color online). Effective dipole mass M_A^{eff} of $F_A(q^2)$ at $m_f = 0.005$, 0.01 together with the experimental result [14]. Result of the dipole fit (solid line) with 1 standard deviation (dashed line) is also presented.

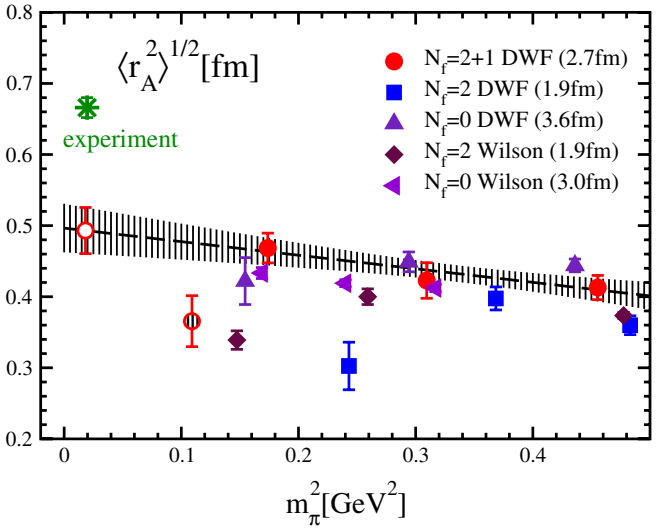

FIG. 25 (color online). Axial charge rms radius $\langle r_A^2 \rangle^{1/2}$ determined from the dipole fit. The dashed line with error band represents a linear extrapolation of our data excluding the lightest point (striped circle). Square, up triangle, diamond, and left triangle denote two-flavor [2] and quenched DWF [1], and two-flavor and quenched Wilson [27] calculations, respectively. The star denotes the experimental result [14].

the dipole form,

$$\frac{F_A(q^2)}{F_A(0)} = \frac{1}{(1 + q^2/M_A^2)^2}, \tag{31}$$

with the experimental data giving a best fit of $M_A = 1.03(2)$ GeV [14] for the axial-vector dipole mass. The experimental fit is shown by the dashed line in Fig. 23.

If the dipole form is valid in the entire q^2 region, we can extract the effective axial dipole mass,

$$M_A^{\text{eff}} = \sqrt{\frac{q^2}{\sqrt{F_A(0)/F_A(q^2)} - 1}} \tag{32}$$

at each nonzero value of q^2. Figure 24 shows that the effective dipole mass at $m_f = 0.01$ is reasonably flat. This means that the form factor behaves as a dipole, as in the cases of the Dirac and Pauli form factors. We fit the form factor with the dipole form, and the fitted dipole mass is consistent with the effective one, as shown in Fig. 24 by the solid line with the 1 standard deviation (dashed lines).

Figure 24 shows that the lightest quark mass data is also well explained by the dipole form, although the results do not approach the experimental value.

The axial rms radius is determined from the dipole mass,

$$\langle r_A^2 \rangle^{1/2} = \sqrt{12}/M_A, \tag{33}$$

and is 0.666(14) fm in the experiment. The calculated axial rms radius from the fits is shown in Fig. 25 plotted as a function of the pion mass squared. The results are summarized in Table VII. While the result increases as the pion mass decreases, the lightest result significantly decreases. This pion mass dependence is similar to that observed in the axial charge in Fig. 8. This, however, is not clear in $F_A(q^2)$ renormalized by $Z_V = 1/F_1(0)$ obtained on our smaller volume as shown in Fig. 26: the data at the lightest quark mass on the smaller volume shows a significant deviation from the larger volume result, but the statistical

TABLE VII. Axial charge rms radius $\langle r_A^2 \rangle^{1/2}$, nucleon-pion coupling $g_{\pi NN}$, and induced pseudoscalar coupling g_P. $g_{\pi NN}$ is calculated with the definition equation (37) and Goldberger-Treiman (GT) relation equation (38) denoted as def. and GT in the table, respectively. The linear fit results at $m_\pi^{\text{phys}} = 135$ MeV obtained without the lightest quark mass are also presented.

m_f	0.005	0.01	0.02	0.03	m_π^{phys}
$\langle r_A^2 \rangle^{1/2}$ [fm]	0.366(36)	0.469(21)	0.423(25)	0.413(17)	0.493(33)
$g_{\pi NN}$ (def.)	8.53(82)	10.38(94)	11.1(1.3)	12.0(1.1)	9.5(1.6)
$g_{\pi NN}$ (GT)	11.84(45)	13.12(47)	12.66(78)	13.56(57)	12.79(79)
g_P	6.71(60)	8.45(71)	10.31(88)	11.93(93)	6.6(1.2)

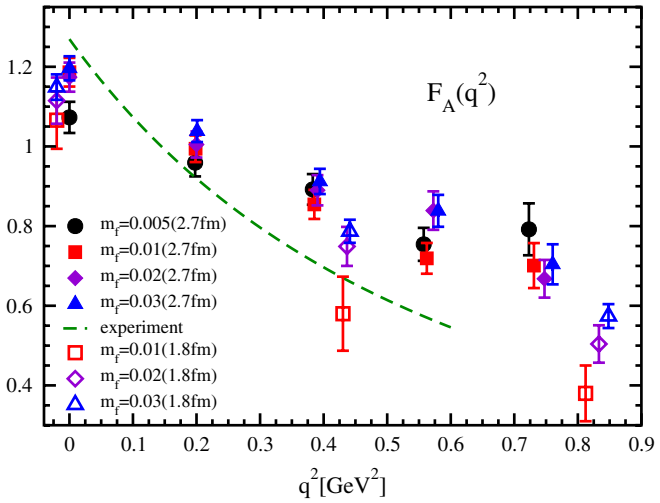

FIG. 26 (color online). Comparison of $F_A(q^2)$ renormalized by $Z_V = 1/F_1(0)$ with larger and smaller volumes denoted by closed and open symbols, respectively, at each quark mass. Open symbols at $q^2 = 0$ are slightly shifted to the minus direction in the x-axis. The dashed curve is a fit to experimental data.

errors are too large to allow for a more quantitative comparison.

Here, we similarly suspect this behavior of the larger volume to be caused by a large finite-volume effect. A similar behavior is also seen in previous two-flavor results as presented in Fig. 25. DWF [2] and Wilson [27] fermion calculations on a smaller volume $(1.9\ \text{fm})^3$ have similar pion mass dependences, but the radius begins to decrease at heavier pion mass. Once again, this behavior is quite similar to the case of the axial charge. Moreover, previous quenched results obtained on large volumes [1,23] do not exhibit such strong pion mass dependence, which is also shown in Fig. 25. Figure 27 shows the same results of the rms radii, but plotted as a function of $m_\pi L$. The scaling of the rms radius with $m_\pi L$ is not as compelling as the axial charge case, but from the figure we estimate that $m_\pi L > 6$ is required to obtain the axial charge rms radius without significant finite-volume effects. Needless to say, other systematic errors, e.g., due to heavier quark mass than the physical one, should be removed to reproduce the experimental value.

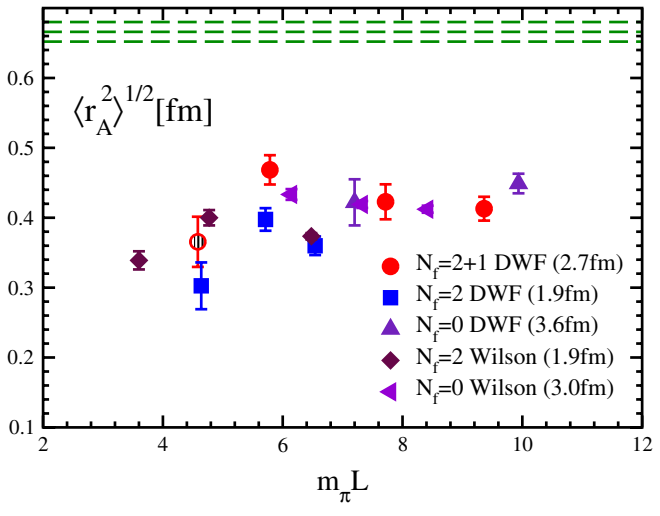

FIG. 27 (color online). Same as Fig. 25 except the horizontal axis is the scaling variable $m_\pi L$. Dashed lines denote the experimental result [14] and its 1 standard deviation.

The lightest pion mass data is omitted in the following chiral extrapolation, because we cannot rule out a large systematic error due to the finite volume of the simulations as discussed above. A linear fit to the heaviest three quark masses and extrapolation to the physical pion mass yields $\langle r_A^2 \rangle^{1/2} = 0.49(3)$ fm. The fit result is presented in Fig. 25 and reproduces 73% of the experimental value.

2. *Induced pseudoscalar form factor* $F_P(q^2)$

The induced pseudoscalar form factor, $F_P(q^2)$, is expected to have a pion pole, so its momentum-transfer dependence should be different from the other form factors. At the lightest quark mass this form factor is suspected to have a large finite-volume effect, since it is obtained from the matrix element of the axial-vector current together with the axial-vector form factor, as discussed in the previous subsection.

Figure 28 shows $2M_N F_P(q^2)$ renormalized with Z_V, plotted against the momentum transfer squared at each quark mass. We immediately notice that this form factor has a much larger q^2 dependence than the other form factors. In addition, the results from all quark masses appear to be consistent with the experimental data [15]. Note that our statistical error is much smaller than the experiment.

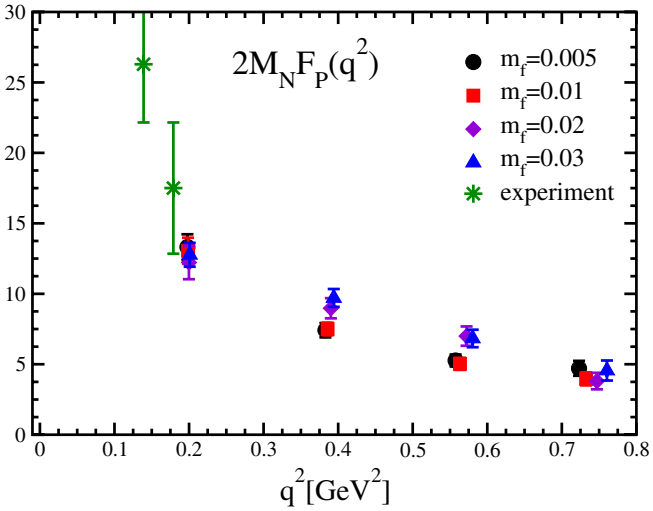

FIG. 28 (color online). $2M_N F_P(q^2)$ renormalized by $Z_V = 1/F_1(0)$ with experimental values [15].

The induced pseudoscalar form factor is related to the axial-vector form factor through the so-called partially conserved axial-vector current (PCAC) relation which is a manifestation of spontaneously broken chiral symmetry. In the traditional PCAC current algebra with pion-pole dominance (PPD), the PPD form,

$$F_P^{\mathrm{PPD}}(q^2) = \frac{2M_N F_A(q^2)}{q^2 + m_\pi^2}, \tag{34}$$

is obtained at $m_\pi \approx 0$. The denominator on the right-hand side of this relation corresponds to the pion pole. We investigate the validity of this relation in our results through a quantity,

$$\alpha_{\mathrm{PPD}} = \frac{(q^2 + m_\pi^2)F_P(q^2)}{2M_N F_A(q^2)}. \tag{35}$$

If the relation holds we obtain unity for this quantity at all q^2. Figure 29 shows α_{PPD} calculated using our lattice results for F_A and F_P. There is no significant q^2 dependence, and while the values are close to unity, they are systematically less than one. We fit these results by a constant for each quark mass, whose results are presented in Fig. 29 and Table VIII. While all the fit results are consistent with the experimental data [15,16,67] within the larger error of the experiments, they are about 10%–20% smaller than the prediction of the PPD form.

We should note that the quantity at the lightest quark mass looks similar to the others, but $F_A(q^2)$ at $m_f = 0.005$ is suspected to have a large finite-volume effect as discussed in the last subsection. This means that $F_P(q^2)$ at $m_f = 0.005$ is expected to suffer from a similarly sized effect at the same quark mass. Thus, it appears that the two large finite-volume effects cancel in this ratio.

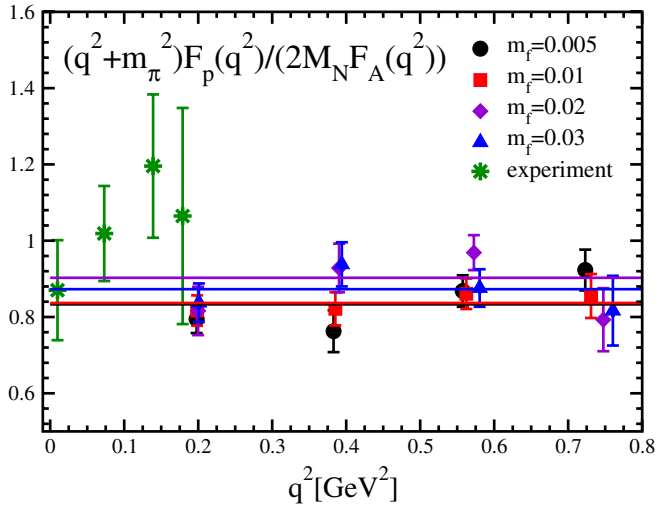

FIG. 29 (color online). Induced pseudoscalar form factor $F_P(q^2)$ normalized by nucleon mass, $F_A(q^2)$, and pion pole, along with experimental values [15].

TABLE VIII. α_{PPD} and $m_{F_P}^{\mathrm{pole}}$.

m_f	0.005	0.01	0.02	0.03
α_{PPD}	0.833(25)	0.837(29)	0.903(32)	0.873(31)
$[m_{F_P}^{\mathrm{pole}}/m_\pi]^2$	1.044(39)	1.009(19)	0.940(24)	0.977(20)

We check the consistency of the pole mass in $F_P(q^2)$ with the measured pion mass at each quark mass by observing that the pole mass is given by

$$(m_{F_P}^{\mathrm{pole}})^2 = \frac{2\alpha_{\mathrm{PPD}} M_N F_A(q^2)}{F_P(q^2)} - q^2, \tag{36}$$

where we use the fact that $\alpha_{\mathrm{PPD}} \neq 1$ in our data. Figure 30 shows that the ratio $[m_{F_P}^{\mathrm{pole}}/m_\pi]^2$ is reasonably consistent with unity and has no large q^2 dependence except for the lightest quark mass point, which has large statistical error. The values obtained from a constant fit are presented in Table VIII. This consistency suggests that $F_P(q^2)$ does indeed have a pion-pole structure, which is consistent with the PPD form, however $\alpha_{\mathrm{PPD}} \neq 1$ in our data. We confirmed that $m_{F_P}^{\mathrm{pole}}$ and α_{PPD} obtained from a monopole fit of $2M_N F_A/F_P$ are reasonably consistent with the above results, but have larger errors.

The pion-nucleon coupling is related to the induced pseudoscalar form factor via the relation

$$g_{\pi NN} = \lim_{q^2 \to -m_\pi^2} \left[\frac{(q^2 + m_\pi^2)F_P(q^2)}{2F_\pi} \right], \tag{37}$$

where $F_\pi = 92.4$ MeV. Combining the above relation with the PPD form, Eq. (34), we obtain the Goldberger-Treiman (GT) relation [13],

$$g_{\pi NN} F_\pi = M_N g_A. \tag{38}$$

In this relation we assume $F_A(0) \approx F_A(-m_\pi^2)$. As such it

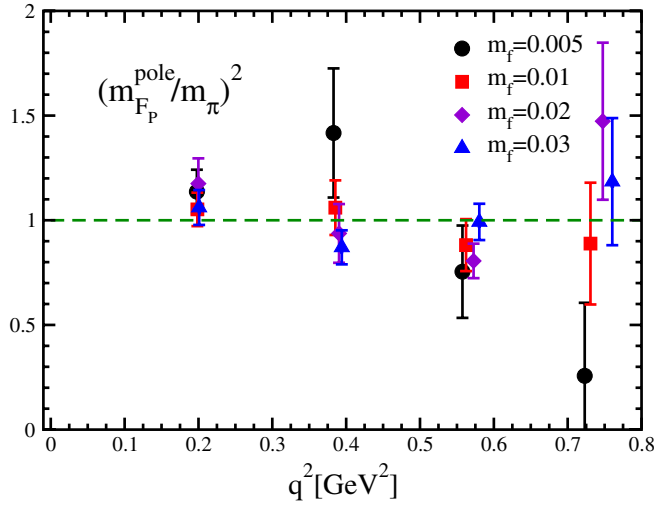

FIG. 30 (color online). Ratio of the pole mass in $F_P(q^2)$ and measured pion mass.

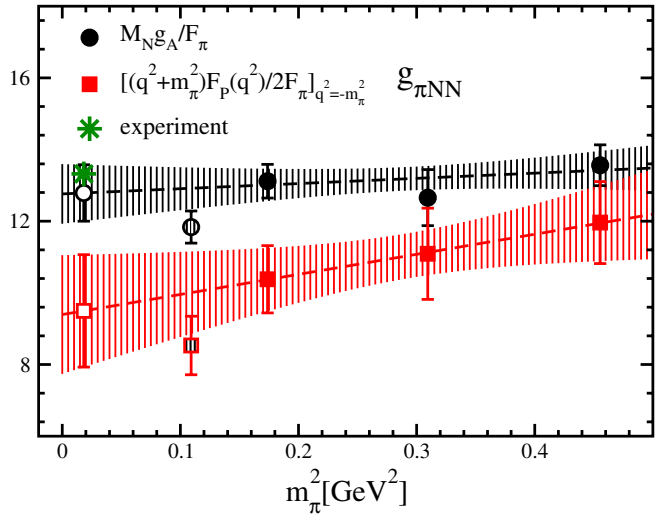

FIG. 31 (color online). Two measurements of the πNN coupling with the Goldberger-Treiman relation and definition of $g_{\pi NN}$. The experimental value [68] is indicated by the star. The dashed lines with error band present linear extrapolations of our data without lightest point.

suffers from a small mismatch in momentum transfer. Nevertheless, if we substitute the experimental values for the quantities, we obtain $g_{\pi NN} = 12.9$.

Figure 31 shows two calculations for the πNN coupling, $g_{\pi NN}$: one uses the definition of $g_{\pi NN}$ and another the GT relation at each quark mass, plotted against the pion mass squared. In determining $g_{\pi NN}$, we use the measured pion decay constant at each quark mass from Ref. [47]. Results for $g_{\pi NN}$ from both methods are given in Table VII. From Fig. 31, we observe that $g_{\pi NN}$ obtained from both methods displays only a mild m_π^2 dependence, with the exception of the lightest mass results which show a significant downward shift away from the trend set by the three heavier mass values. This of course is another manifestation of the large finite-size effect observed in the axial charge (see Sec. IV A). Hence, for the chiral extrapolation we simply employ a linear fit form and exclude the lightest mass point. We obtain the results at the physical pion mass, $g_{\pi NN} = 9.5(1.6)$ from the definition equation (37), and $g_{\pi NN} = 12.8(8)$ from the GT relation equation (38). The value obtained using the GT relation agrees with a recent estimation of the coupling $g_{\pi NN} = 13.3(9)$ obtained from forward πN scattering data [68], and also with the previous result, $g_{\pi NN} = 11.8(3)$, from a quenched simulation performed using the Wilson action [27] estimated by the GT relation. The result from the definition equation (37), on the other hand, is consistent with a quenched DWF determination, $g_{\pi NN} = 10.4(1.0)$ [1], obtained from $F_P(-m_\pi^2)$.

Rigorously speaking, the GT relation is not valid in our data, since our data do not satisfy the PPD form due to $\alpha_{\mathrm{PPD}} \approx 0.85$. Thus, the difference between the two determinations of $g_{\pi NN}$ can be explained by α_{PPD}. Further study of the GT relation is an important future work, since the relation should be satisfied in the chiral limit, and at zero momentum transfer.

The induced pseudoscalar coupling for muon capture on the proton, $g_P = m_\mu F_P(q_c^2)$ where $q_c^2 = 0.88 m_\mu^2$, is defined with the muon mass m_μ and the induced pseudoscalar form factor F_P at the specific momentum transfer where the muon capture occurs, $p + \mu^- \rightarrow n + \nu_\mu$.

Since $F_P(q^2)$ has significantly large pion mass and momentum-transfer dependences due to the pion pole, we subtract this contribution before performing the momentum transfer and chiral extrapolations. To do this, we first define the quantity with pion-pole subtraction by

$$\bar{F}_P(q^2) = (q^2 + m_\pi^2) F_P(q^2) \tag{39}$$

at each q^2 and then extrapolate this to the required momentum transfer q_c^2. The induced pseudoscalar coupling is estimated by the normalization factor with the physical pion mass

$$g_p = m_\mu \frac{\bar{F}_P(q_c^2)}{q_c^2 + (m_\pi^{\mathrm{phys}})^2}, \tag{40}$$

where $m_\pi^{\mathrm{phys}} = 135$ MeV, at each quark mass as shown in Fig. 32. The figure shows that the result is almost linear as a function of the pion mass squared and decreases toward the experimental result for the three heavier mass values. Again the lightest mass result is an exception caused by the finite-volume effect in g_A, as discussed in Sec. IV A. The result at the physical pion mass, presented in Table VII, is obtained from a linear fit to the heaviest three pion masses and is consistent with the recent experiment [16] and analysis [67]. This result also agrees with the

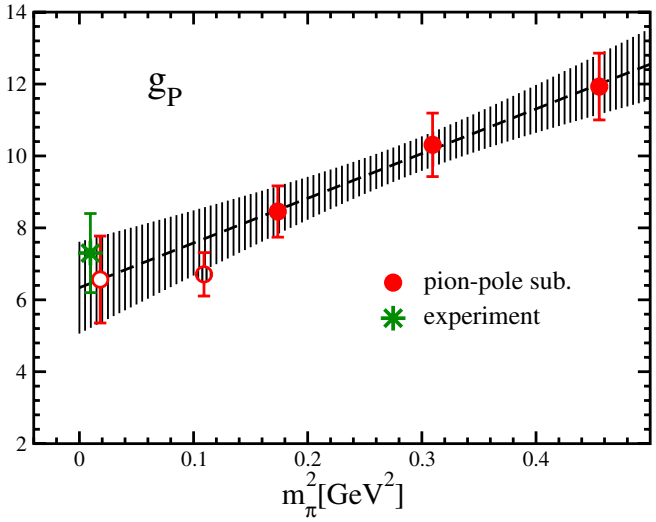

FIG. 32 (color online). Induced pseudoscalar coupling for muon capture, g_p, estimated with pion-pole subtraction. The experimental result [16] is indicated by the star. The dashed line with error band represents a linear extrapolation of our data excluding the lightest point.

previous quenched DWF result [1], while it disagrees with a quenched Wilson determination [27,69] which is almost half of the experimental value.

V. CONCLUSIONS

We have studied the isovector nucleon form factors with $N_f = 2 + 1$ flavors of dynamical quarks using the domain-wall fermion action at a lattice cutoff of $a^{-1} = 1.73$ GeV. The form factors are calculated with four light quark masses, corresponding to a lightest pion mass, $m_\pi = 0.33$ GeV, and with momentum transfers down to $q^2 \approx 0.2$ GeV^2.

We have found the axial charge decreases significantly at the lightest quark mass point on the larger volume while the effect sets in for heavier quark mass on the smaller volume. By comparing our results with those using different volumes, numbers of flavors, and lattice fermions as a function of the single variable $m_\pi L$, we conclude that this downward trend is caused by the finite volume used in our calculation. The fact that such an effect is absent in quenched and partially quenched mixed-action studies on large volumes may be explained by the presence of unphysical logarithms.

We have fit the data to several forms, including finite-volume effects, and obtain $g_A = 1.19(6)(4)$, where the first and second errors are statistical and systematic, respectively, which is 7% smaller than the experimental value. In our estimation, a spatial volume of $V \geq (3.5\ \text{fm})^3$ is required to keep the finite-volume effect at or below 1% at $m_\pi = 0.33$ GeV. Hence lattice calculations should continue to push down the quark mass and increase the volume with $m_\pi L > 6$. Detailed analyses of the quark mass and finite-volume dependence is desirable to understand the systematic deviation from the experiment.

Our lattice results for the form factors of the vector current are well fit by the standard dipole form. We have evaluated the root-mean-squared radii and the difference of the anomalous magnetic moment between the proton and neutron from the dipole fits. The radii and the anomalous moment are well explained by a linear function of the pion mass squared. In the radii we have not observed divergent quark mass behaviors predicted by HBChPT. Besides the divergent behavior, the pion mass dependences for the observables are quite consistent with other lattice QCD calculations including the recent results of LHP. Because of the linear behavior, we have concluded that the form factors of the vector current are less sensitive to the finite-volume effect in contrast to the axial charge. Although both Dirac and Pauli rms radii approach to the experimental values as the pion mass decreases, the values extrapolated by the linear form at the physical pion mass underestimate the experiments by about 25%. Future work will involve simulating at lighter quark masses to search for the non-analytic behavior predicted by HBChPT.

The axial-vector form factor is also well described by the dipole form, even at the lightest quark mass, where the axial charge, $F_A(0)$, is suspected to have a large finite-volume effect. The axial charge radius, obtained from the dipole fit, has a downward tendency as a function of the pion mass squared, which drives the radius away from the experimental value. We have considered this dependence to be caused by the finite volume of our simulation, as in the case of the axial charge. We observe that our results seem to scale as $m_\pi L$, as do previous calculations using several volumes. We have concluded that the form factors of the axial-vector current are more sensitive to the finite volume than those of the vector current from the observations of the finite-volume effects.

We have checked the pion-pole structure in the induced pseudoscalar form factor with our simulations. We have found that the pion-pole dominance form describes our data well, with the exception that $\alpha_{\text{PPD}} < 1$. Taking into account that $\alpha_{\text{PPD}} \neq 1$, the pole mass of the induced pseudoscalar form factor reasonably agrees with the measured pion mass.

For a precision test of QCD from nucleon matrix elements, we have identified several problems that first need to be overcome, such as finite-volume systematic errors in the axial charge and the form factors of the axial-vector currents, and the underestimation of the radii of the form factors of the vector current. Further lighter quark mass and larger volume calculations are essential to solve the problems, and such simulations are underway. Besides the comparisons with the experimental values, it is also important future work to study why α_{PPD} deviates from unity.

ACKNOWLEDGMENTS

We thank the members of the RIKEN-BNL-Columbia (RBC) and UKQCD Collaborations. We also thank RIKEN, Brookhaven National Laboratory, the U.S. Department of Energy, Edinburgh University, and the U.K. PPARC for providing the facilities essential for the completion of this work. T. B. and T. Y. were supported by the U.S. DOE under Contract No. DE-FG02-92ER40716. T. Y. was supported by the Yukawa Memorial Foundation. H. L. is supported by DOE Contract No. DE-AC05-06OR23177 under which JSA, LLC operates THNAF. S. S. is supported by JSPS Grant-In-Aid for Scientific Research (C) (No. 19540265). J. Z. is supported by STFC Grant No. PP/F009658/1.

[1] S. Sasaki and T. Yamazaki, Phys. Rev. D **78**, 014510 (2008).
[2] H.-W. Lin, T. Blum, S. Ohta, S. Sasaki, and T. Yamazaki (RBC Collaboration), Phys. Rev. D **78**, 114505 (2008).
[3] J. Arrington, C. D. Roberts, and J. M. Zanotti, J. Phys. G **34**, S23 (2007).
[4] R. Hofstadter and R. W. McAllister, Phys. Rev. **98**, 217 (1955).
[5] F. Bumiller, M. Croissiaux, and R. Hofstadter, Phys. Rev. Lett. **5**, 261 (1960).
[6] F. Bumiller, M. Croissiaux, E. Dally, and R. Hofstadter, Phys. Rev. **124**, 1623 (1961).
[7] T. Janssens, R. Hofstadter, E. B. Hughes, and M. R. Yearian, Phys. Rev. **142**, 922 (1966).
[8] M. K. Jones *et al.* (Jefferson Lab Hall A), Phys. Rev. Lett. **84**, 1398 (2000).
[9] O. Gayou *et al.* (Jefferson Lab Hall A), Phys. Rev. Lett. **88**, 092301 (2002).
[10] Y. Nambu and G. Jona-Lasinio, Phys. Rev. **122**, 345 (1961).
[11] Y. Nambu and G. Jona-Lasinio, Phys. Rev. **124**, 246 (1961).
[12] C. Amsler *et al.* (Particle Data Group), Phys. Lett. B **667**, 1 (2008).
[13] M. L. Goldberger and S. B. Treiman, Phys. Rev. **110**, 1178 (1958).
[14] V. Bernard, L. Elouadrhiri, and U. G. Meissner, J. Phys. G **28**, R1 (2002).
[15] S. Choi *et al.*, Phys. Rev. Lett. **71**, 3927 (1993).
[16] V. A. Andreev *et al.* (MuCap Collaboration), Phys. Rev. Lett. **99**, 032002 (2007).
[17] P. Hagler, Proc. Sci., LAT2007 (2007) 013.
[18] J. M. Zanotti, Proc. Sci., LAT2008 (2008) 007.
[19] M. Gockeler *et al.* (QCDSF Collaboration), Phys. Rev. D **71**, 034508 (2005).
[20] S. Sasaki, K. Orginos, S. Ohta, and T. Blum (RBCK Collaboration), Phys. Rev. D **68**, 054509 (2003).
[21] A. Tang, W. Wilcox, and R. Lewis, Phys. Rev. D **68**, 094503 (2003).
[22] S. Boinepalli, D. B. Leinweber, A. G. Williams, J. M. Zanotti, and J. B. Zhang, Phys. Rev. D **74**, 093005 (2006).
[23] C. Alexandrou, G. Koutsou, J. W. Negele, and A. Tsapalis, Phys. Rev. D **74**, 034508 (2006).
[24] A. A. Khan *et al.*, Phys. Rev. D **74**, 094508 (2006).
[25] M. Gockeler *et al.* (QCDSF/UKQCD Collaboration), Proc. Sci., LAT2007 (2007) 161.
[26] R. G. Edwards *et al.* (LHP Collaboration), Phys. Rev. Lett. **96**, 052001 (2006).
[27] C. Alexandrou *et al.*, Phys. Rev. D **76**, 094511 (2007).
[28] P. Hagler *et al.* (LHP Collaboration), Phys. Rev. D **77**, 094502 (2008).
[29] J. D. Bratt *et al.*, Proc. Sci., LATTICE2008 (2008) 141.
[30] C. Alexandrou *et al.*, Phys. Rev. D **77**, 085012 (2008).
[31] D. Guadagnoli, V. Lubicz, M. Papinutto, and S. Simula, Nucl. Phys. **B761**, 63 (2007).
[32] S. Sasaki and T. Yamazaki, Phys. Rev. D **79**, 074508 (2009).
[33] H.-W. Lin and K. Orginos, Phys. Rev. D **79**, 074507 (2009).
[34] P. H. Ginsparg and K. G. Wilson, Phys. Rev. D **25**, 2649 (1982).
[35] D. B. Kaplan, Phys. Lett. B **288**, 342 (1992).
[36] D. B. Kaplan, Nucl. Phys. B, Proc. Suppl. **30**, 597 (1993).
[37] Y. Shamir, Nucl. Phys. **B406**, 90 (1993).
[38] V. Furman and Y. Shamir, Nucl. Phys. **B439**, 54 (1995).
[39] T. Yamazaki *et al.* (RBC and UKQCD Collaborations), Phys. Rev. Lett. **100**, 171602 (2008).
[40] T. Yamazaki and S. Ohta (RBC and UKQCD Collaborations), Proc. Sci., LAT2007 (2007) 165.
[41] S. Ohta and T. Yamazaki (RBC and UKQCD Collaborations), Proc. Sci., LAT2008, 168 (2008).
[42] S. Sasaki, T. Blum, and S. Ohta, Phys. Rev. D **65**, 074503 (2002).
[43] K. Sasaki and S. Sasaki, Phys. Rev. D **72**, 034502 (2005).
[44] C. Alexandrou, S. Gusken, F. Jegerlehner, K. Schilling, and R. Sommer, Nucl. Phys. **B414**, 815 (1994).
[45] W. Wilcox, T. Draper, and K.-F. Liu, Phys. Rev. D **46**, 1109 (1992).
[46] P. Hagler *et al.* (LHP Collaboration), Phys. Rev. D **68**, 034505 (2003).
[47] C. Allton *et al.* (RBC and UKQCD Collaborations), Phys. Rev. D **78**, 114509 (2008).
[48] Y. Iwasaki (unpublished).
[49] F. Berruto, T. Blum, K. Orginos, and A. Soni, Phys. Rev. D **73**, 054509 (2006).
[50] A. W. Thomas, J. D. Ashley, D. B. Leinweber, and R. D. Young, J. Phys. Conf. Ser. **9**, 321 (2005).
[51] D. Dolgov *et al.* (LHP Collaboration), Phys. Rev. D **66**, 034506 (2002).
[52] M. Kim and S. Kim, Phys. Rev. D **58**, 074509 (1998).
[53] O. Bar *et al.*, Phys. Rev. D **72**, 054502 (2005).
[54] S. Prelovsek, Phys. Rev. D **73**, 014506 (2006).
[55] F.-J. Jiang, arXiv:hep-lat/0703012.
[56] J.-W. Chen, D. O'Connell, and A. Walker-Loud, J. High Energy Phys. 04 (2009) 090.
[57] W. Detmold and M. J. Savage, Phys. Lett. B **599**, 32 (2004).
[58] B. Smigielski and J. Wasem, Phys. Rev. D **76**, 074503 (2007).
[59] V. Bernard and U.-G. Meissner, Phys. Lett. B **639**, 278 (2006).
[60] R. L. Jaffe, Phys. Lett. B **529**, 105 (2002).
[61] S. R. Beane and M. J. Savage, Phys. Rev. D **70**, 074029 (2004).
[62] W. Detmold and C.-J. D. Lin, Phys. Rev. D **71**, 054510 (2005).
[63] S. N. Syritsyn *et al.* (LHP Collaboration), Proc. Sci., LATTICE2008 (2008) 169.
[64] M. A. B. Beg and A. Zepeda, Phys. Rev. D **6**, 2912 (1972).
[65] V. Bernard, H. W. Fearing, T. R. Hemmert, and U. G. Meissner, Nucl. Phys. **A635**, 121 (1998).
[66] P. Wang, D. B. Leinweber, A. W. Thomas, and R. D. Young, Phys. Rev. D **79**, 094001 (2009).
[67] A. Czarnecki, W. J. Marciano, and A. Sirlin, Phys. Rev. Lett. **99**, 032003 (2007).
[68] T. E. O. Ericson, B. Loiseau, and A. W. Thomas, Phys. Rev. C **66**, 014005 (2002).
[69] The value is estimated by the authors of Ref. [1] using the raw data in Ref. [27].